

Engineering Impacts of the August 4, 2020 Port of Beirut, Lebanon Explosion



A report of the NSF-Sponsored Geotechnical Extreme Event Reconnaissance Association in
Collaboration with the American University of Beirut

Salah Sadek, Mayssa Dabaghi, and Imad Elhajj, Maroun Semaan Faculty of Engineering and Architecture,
American University of Beirut, Lebanon

Paolo Zimmaro, University of Calabria, Italy; University of California, Los Angeles

Youssef M.A. Hashash, University of Illinois at Urbana-Champaign

Sang-Ho Yun, Jet Propulsion Laboratory, California Institute of Technology, Pasadena, CA

Timothy M. O'Donnell and Jonathan P. Stewart, University of California, Los Angeles

Report GEER-070: <https://doi.org/10.18118/G6C96C>

February 4 2021

Table of Contents

Table of Contents

List of Figures

List of Tables

Report Contributors

Report Reviewers

Executive Summary

1.0 Introduction	1
2.0 External Information and Data Sources	5
2.1 Beirut Base Maps	5
2.2 Damage Proxy Maps	5
2.3 Order of Engineers Damage Inspections	6
2.4 Open Map Lebanon	9
3.0 Impact on Port of Beirut	10
3.1 Description of Port Facility	10
3.2 Explosion Impacts	18
3.2.1 <i>Grain Silos</i>	19
3.2.2 <i>Ground Zero Crater</i>	25
3.2.2 <i>Other Ground Movements and Observations Across Port Complex</i>	32
4.0 Impacts on Buildings	39
4.1 In-Person Building Inspections	40
4.2 Street-View Photo Survey	43
4.3 Structural Damage Assessment	45
4.3.1 <i>Damage Re-Classification</i>	45
4.3.2 <i>Examples of Damage Buildings</i>	47
4.3.3 <i>Summary and Interpretation</i>	59
4.4 Façade Damage Assessment	60
4.4.1 <i>Damage Classification</i>	60
4.4.2 <i>Results</i>	61
4.5 Comparison of Damage Observations to DPMs	63

5.0 Summary and Research Opportunities	66
References	67
Appendix	69

List of Figures

Figure 1.1 Map of Beirut showing radial lines from Ground Zero at Hangar 12.	1
Figure 1.2 Time-lapse photography of the blast plume as viewed from the west.	2
Figure 1.3 Time-lapse photography of the blast plume as viewed from the south.	3
Figure 2.1 DPM produced following the 4 August, 2020 blast explosion.	6
Figure 2.2 Locations of buildings in Beirut surveyed by OEA following August 4, 2020 blast.	7
Figure 2.3 Conditions of buildings surveyed surveyed by OEA.	7
Figure 2.4 Conditions of heritage buildings surveyed by OEA.	8
Figure 2.5 OEA recommendations on actions to be taken for surveyed buildings.	8
Figure 3.1 Scaled representation of Beirut Port expansion from 1875 to 2020	10
Figure 3.2 Works on the Beirut Port expansion in 1886.	11
Figure 3.3 Phase I grain silos completed and Phase II nearing completion.	12
Figure 3.4 Plan view showing the grain silo complex with all three phases completed.	13
Figure 3.5 Grain silo foundation construction: Casting of 30x30 cm square reinforced concrete piles and pile driving.	13
Figure 3.6 Excavation for the silos base slabs and exposing the pile heads prior to casting of the caps.	14
Figure 3.7 Copy of original foundation plans.	15
Figure 3.8 Only available information re. the foundation materials in the silos zone.	15
Figure 3.9 Coring through one of the “intact” cells.	16
Figure 3.10 Aerial view of Port of Beirut prior to 4 August 2020 explosion.	17
Figure 3.11 Basin 3 and associated quays.	18
Figure 3.12 Plan view of the silos and Hangar 12 in June 2020.	19
Figure 3.13 Image taken from a drone looking towards the west.	20
Figure 3.14 Schematic of damage levels observed on site.	20
Figure 3.15 Processed image from drone-mountain LiDAR scan.	21
Figure 3.16 Frontal view of silos looking towards the west.	21

Figure 3.17 Close-up view of the destroyed and severely damaged silos that were empty at the time of the 4 August 2020 explosion.	22
Figure 3.18 Picture taken from the seaside close to Quay 8 looking south towards the city.	23
Figure 3.19 Complete failure/crushing of the concrete and collapse of the shell structures..	23
Figure 3.20 View of the third row of silos on the opposite side of the explosion source.	24
Figure 3.21 Horizontal deflections of west side of silos as evaluated from LiDAR point cloud data.	25
Figure 3.22 Aerial views of ground zero (Hangar 12) prior to (31 July 2020) and immediately following (4 August 2020) the explosion.	26
Figure 3.23 Superimposed Google Earth images from 31 July 2020 and 5 August 2020.	27
Figure 3.24 Top: Superposition of bathymetry survey on Google Earth image of crater and adjacent area; Bottom: Water depths from bathymetric survey and approximate limit of depth decrease from flow slide.	28
Figure 3.25 Depth contours in the crater area.	29
Figure 3.26 Isometric view of surface revealed by bathymetric survey.	30
Figure 3.27 Schematic of a pre and post event section through the crater.	31
Figure 3.28 Screen shot from Solidworks software showing the 3D volumes analyzed.	32
Figure 3.29 Reference map for the observations and pictures included in this section.	33
Figure 3.30 Ground deformation and mini-cratering exposed by truck traffic and possibly resulting from loosening and/or shifting of the fill below.	33
Figure 3.31 Surface expressions similar to Figure 3.30 at a location close-by.	34
Figure 3.32 Dock along Quay 10.	34
Figure 3.33 Close-up of the void below the asphalted section/pavement.	35
Figure 3.34 Medium-sized vessel that was docked at Quay 9, lifted by the water wave generated by the explosion and left on the dock at Quay 10.	35
Figure 3.35 Closer view of the vessel with evidence of the indentation caused by the pressure wave.	36
Figure 3.36 No evidence of damage to the western section of Quay 10.	36
Figure 3.37 Typical damage done to steel structures throughout the Port.	37
Figure 3.38 Piles driving in Container Terminal portion of Port of Beirut as part of 2011 expansion.	38
Figure 4.1 Buildings inspected by MSFEA as part of the GEER reconnaissance.	41
Figure 4.2 Tracklog of street-view photo survey undertaken on 8 and 15 October 2020.	43

Figure 4.3 Example images from street-view photo survey as captured (left) and as viewed using the GoPro VR player (right).	44
Figure 4.4 Locations of example stone masonry (SM) and reinforced concrete (RC) structures with varying levels of structural damage.	47
Figure 4.5 Set of buildings with varying structural typologies and damage classes.	48
Figure 4.6 Heavily damaged stone masonry buildings classified based on 360° photos.	49
Figure 4.7 Partially collapsed (D4) stone masonry building SM4.	50
Figure 4.8 Partially collapsed (D4) stone masonry building SM5.	51
Figure 4.9 Heavily damaged (D3) stone masonry building SM6.	52
Figure 4.10 Another example of a heavily damaged (D3) stone masonry building SM7.	53
Figure 4.11 Example observations from moderately damaged (D2) stone masonry buildings SM8 and SM9.	54
Figure 4.12 Heavily damaged (D3) older reinforced concrete building RC1.	55
Figure 4.13 Moderately damaged (D2) new reinforced concrete building RC2.	56
Figure 4.14 Heavily damaged (D3) older reinforced concrete building RC3 in poor condition before the blast.	58
Figure 4.15 Distribution of damage classes in (a) Stone Masonry and (b) Reinforced Concrete buildings.	59
Figure 4.16 Distribution of classified buildings with blast distance.	60
Figure 4.17 Example of façade damage levels.	62
Figure 4.18 Non-structural damage assessment map.	62
Figure 4.19 DPM and structural damage category distributions across Beirut.	63
Figure 4.20 Relationship between numerical index of DPM (0-1) and structural damage categories.	64
Figure 4.21 DMP and non-structural damage assessment map.	65
Figure 4.22 Relationship between numerical index of DMP (0-1) and non-structural damage categories.	65
Figure A-1 Part 1 of the MSFEA assessment form on ArcGIS Survey123 (ESRI).	69
Figure A-2 Part 2 of the MSFEA assessment form on ArcGIS Survey123 (ESRI).	70
Figure A-3 Part 3 of the MSFEA assessment form on ArcGIS Survey123 (ESRI).	71
Figure A-4 Part 4 of the MSFEA assessment form on ArcGIS Survey123 (ESRI).	72

Figure A-5 Part 5 of the MSFEA assessment form on ArcGIS Survey123 (ESRI).	73
Figure A-6 Part 6 of the MSFEA assessment form on ArcGIS Survey123 (ESRI).	74

List of Tables

Table 4.1 Characteristics of the Beirut building stock (adapted from Salameh et al. 2016)	39
Table 4.2 Building safety classification applied during MSFEA building inspections. Adapted from ATC-20 (1995) and ATC-45 (2004).	42
Table 4.3 Structural damage classifications. Adapted from Bray & Stewart (2000) & EMS98 (Grünthal, 1998)	45-46
Table 4.4 Characteristics of the Beirut building stock (adapted from Salameh et al. 2016)	61

Acknowledgments

The work of the GEER Association, in general, is based upon work supported in part by the National Science Foundation through the Geotechnical Engineering Program under Grant No. CMMI-1826118. Any opinions, findings, and conclusions or recommendations expressed in this material are those of the authors and do not necessarily reflect the views of the NSF. Any use of trade, firm, or product names is for descriptive purposes only and does not imply endorsement by the U.S. Government. The GEER Association is made possible by the vision and support of the NSF Geotechnical Engineering Program Directors: Dr. Richard Frigaszy and the late Dr. Cliff Astill. GEER members also donate their time, talent, and resources to collect time-sensitive field observations of the effects of extreme events.

Partial support for the work presented here was provided by the Jet Propulsion Laboratory, California Institute of Technology under contract with NASA Earth Applied Sciences Disasters Program.

The authors would like to thank the many entities and individuals that contributed to the information provided in this report. These include the Order of Engineers and Architects of Beirut (OEA) that generously shared the results of their field surveys and preliminary assessment of structures; the Ministry of Commerce and the Beirut Port authority for allowing us access to the facility and sharing available bathymetric and other data; the Universite Saint Joseph School of Engineering and Eng. Emmanuel Durand (Amann Eng. Switzerland) for the laser scanning data/figures of the port silos, the American University of Beirut Maroun Semaan Faculty of Engineering and Architecture (MSFEA) for their support and access to personnel and resources; the AUB-ASCE student chapter and the many volunteers among graduate students, faculty and staff of the MSFEA who led and participated in the rapid assessment surveys and street level 360° mapping.

In particular, for their support of the field reconnaissance, we would like to thank Professors Mounir Mabsout, Georges Saad, Bilal Hamad, Elie Hantouche, Amer El Souri and Elie Shammas; Helmi El Khatib and Dima Al Hassanieh (from the AUB CEE Labs); Roba Houhou, Abed Mikati, Mohamad Antar (Graduate research assistants in GeoEngineering); Dr. Hussein Kassem (AUB alumnus); Karen El Hachem, Nazek Naja and Ghadi El Ghaddaf (AUB undergraduate students). From the AUB Urban Lab, we are grateful to the following individuals who provided access to map products and cadastral and related data: Prof. Mona Fawaz and Eng. Shareef Tarhini. From the University of Illinois at Urbana-Champaign, we thank students Hao Chen and Jack Lawrence for their contributions to image analysis for the assessments of facade damage.

Jungkyo Jung (Jet Propulsion Laboratory, California Institute of Technology, Pasadena, CA) and Cheryl Tay and Emma Hill (Earth Observatory of Singapore, Nanyang Technological University, Singapore) assisted with the generation of Damage Proxy Maps, which is appreciated.

1.0 Introduction

At 18:08 on 4 August 2020, a large explosion occurred at Hangar 12 in the Port of Beirut, Lebanon. The size of the explosion was equivalent to that of an earthquake with local magnitude (M_L) of 3.3 (per [USGS](#)), with an associated best-estimate yield of 0.50 kt TNT (Rigby et al. 2020; Diaz 2020). As such, it is among the most powerful non-nuclear explosions in history (Reuters, 2020). The explosion was preceded by a fire in Hangar 12 and was attributed to the detonation of several hundred tons of ammonium nitrate stored in questionable conditions in that facility. Figure 1.1 shows a map of Beirut marking the location of the port and the surrounding region. The location of Hangar 12 is marked on this map as *Ground Zero*. Several significant structures, including a grain silo immediately west of Hangar 12, are noted in this map. Figures 1.2-1.3 show time-lapse photography of the blast plume as documented from the west and south, respectively.

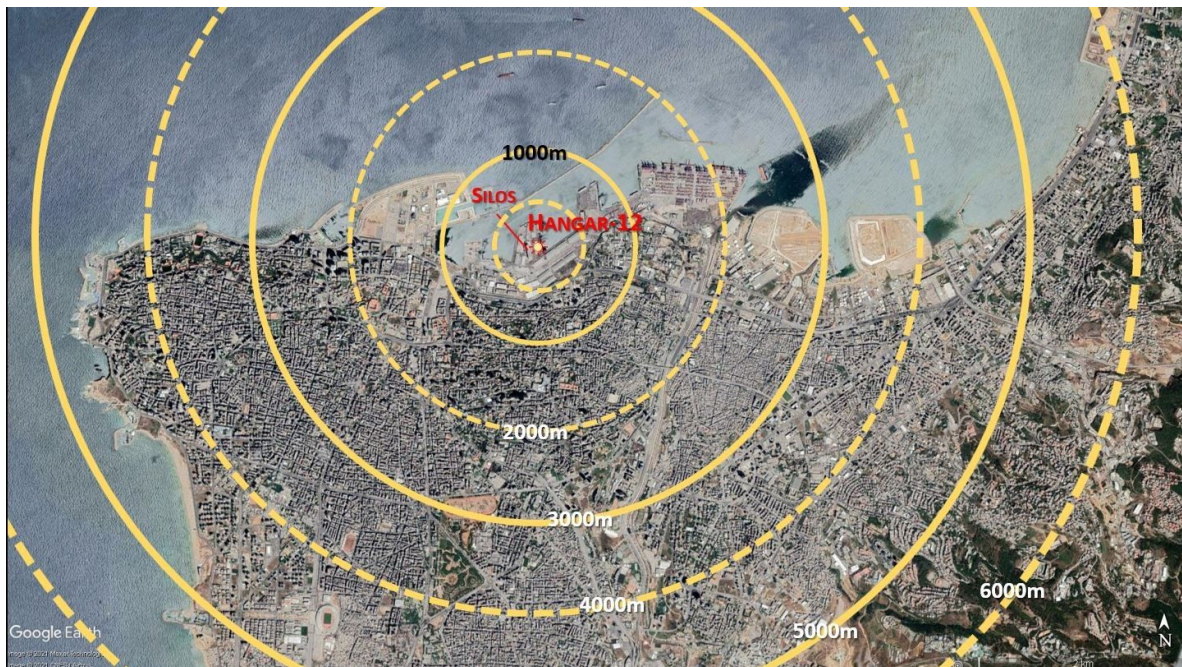


Figure 1.1. Map of Beirut showing radial lines from ground zero at Hangar 12.

Following the event, several organizations mobilized to examine its impact. The Order of Engineers and Architects of Beirut (OEA) undertook building inspections with the aim of identifying structures unsafe for human occupancy (OEA, 2020). Targeted detailed damage surveys were conducted at specific locations by teams of faculty and students of the Civil and Environmental Engineering Dept at the American University of Beirut. The AUB Urban Lab (AUB-UL) engaged with OEA, AUB-MSFEA and several outside agencies including Rice University Spatial Studies Lab and OpenMap Lebanon to [map](#) the impacts of the explosion. The basis for

this mapping was generally rapid visual assessments of buildings conducted to provide advice to Beirut residents and businesses concerned about the structural safety of their buildings.



Figure 1.2. Time-lapse photography of the blast plume as viewed from the west. Source Video-Tweet by Abir Ghattas: <https://twitter.com/AbirGhattas/status/1290671474269986822>

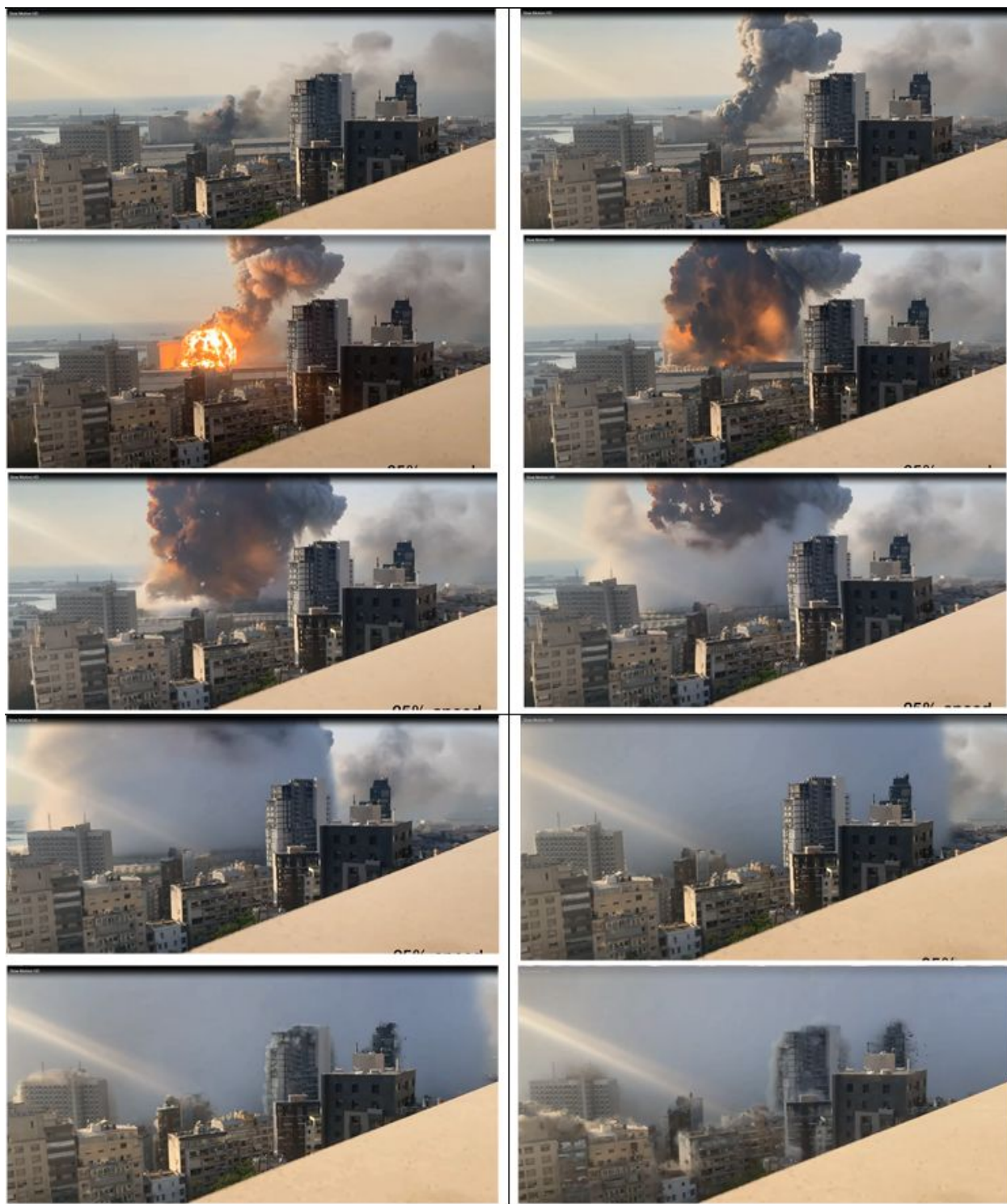


Figure 1.3. Time-lapse photography of the blast plume as viewed from the south. Source video (by Agoston Nemeth): <https://www.youtube.com/watch?v=0tQ80Sj3QUs>

Under the auspices of the NSF-sponsored Geotechnical Extreme Events Reconnaissance Association (GEER), a reconnaissance team was formed in August 2020 to examine the engineering impacts of the explosion with the aim of collecting and documenting perishable data. As the impact of the event unfolded in the ensuing months, our efforts focused on two main effects of the event:

1. The near-field impact of the explosion on Port of Beirut infrastructure, including apparent foundation deformations of the grain silos, flow failures of artificial fill at Ground Zero, and ground deformations in surrounding areas of the port possibly associated with soil failure.
2. The spatially variable impacts of the explosion on buildings in Beirut. Our interest was in documenting distributions of structural damage (i.e., affecting load-bearing elements) and non-structural damage to exterior (facade) elements such as windows and doors.

The principal motivations of this effort were to facilitate subsequent research that could utilize this perishable data. Examples of such research include studies of how effectively satellite-based damage proxy maps (Fielding et al., 2005; Yun et al., 2011) can identify and distinguish different damage levels and studies of blast-impact of varying severity on structures.

Subsequent chapters in this report describe the external information sources utilized in this work, describe the explosion impacts in the Port of Beirut, and describe the explosion impacts on buildings in Beirut. The report is concluded with a description of anticipated future work.

2.0 External Information and Data Sources

This chapter describes information sources external to the GEER reconnaissance and data collection activities. Data collection undertaken as part of the present work is described in Chapters 3-4.

2.1 Beirut Base Maps

We utilize map resources from the AUB [Urban Lab](#) (AUB-UL), which is a collaborative and interdisciplinary research space. The Lab produces scholarship on urbanization by documenting and analyzing ongoing transformation processes in Lebanon in the natural and built environments. The AUB-UL generated and maintains a baseline GIS map for Beirut, among other projects. This curated database includes all cadastral information, buildings, roads, population and other-related data.

The AUB-UL GIS map for Beirut includes information on buildings in the city, including their location, approximate size, and date of construction. This information was derived from public sources, such as assessor files. Buildings in the AUB-UL inventory are shown in Figure 1.1 and subsequent figures in this report.

2.2 Damage Proxy Maps

Remote sensing data represents an invaluable resource when analyzing the effects of natural and/or anthropogenic disasters. In recent years, many investigators used pre- and post-disaster satellite and/or radar data to generate real- or near real-time damage maps. Such remote sensing based multi-epoch post-disaster damage detection techniques were successfully used after various recent earthquakes (e.g., Rathje and Franke, 2016; Jung and Yun, 2020). Following major disasters, the Advanced Rapid Imaging and Analysis (ARIA) team at the California Institute of Technology (Caltech) and the NASA—Jet Propulsion Laboratory (JPL) produce Synthetic Aperture Radar (SAR)-based damage proxy maps (DPMs). Such maps are produced using pre- and post-disaster radar data. The technique used to produce DPMs is based on differences in phase statistics of microwaves returning to a moving platform. In the case of the DPMs, these platforms are satellites (e.g., Fielding et al., 2005; Yun et al., 2011; Yun et al., 2015).

Following the August 4, 2020 Beirut explosion, a DPM was produced using satellite radar data from the Copernicus Sentinel-1 satellites. This DPM was generated comparing pre- and post-explosion SAR scenes acquired from four different tracks. Two of the satellite tracks were oriented looking from west, while two of them from east, with look-angles from vertical ranging between 31°-44°. The map used 12 pre-event and two post-event SAR scenes between May 1, 2020 and September 1, 2020. The map covers an area of 13 by 16 km (Figure 2.1). Each colored pixel measures about 10 by 10 meters. Colored pixels represent zones where there was significant change in radar wave scattering at the reflectors (i.e., ground surface or buildings), which may indicate damage from the stressing event.

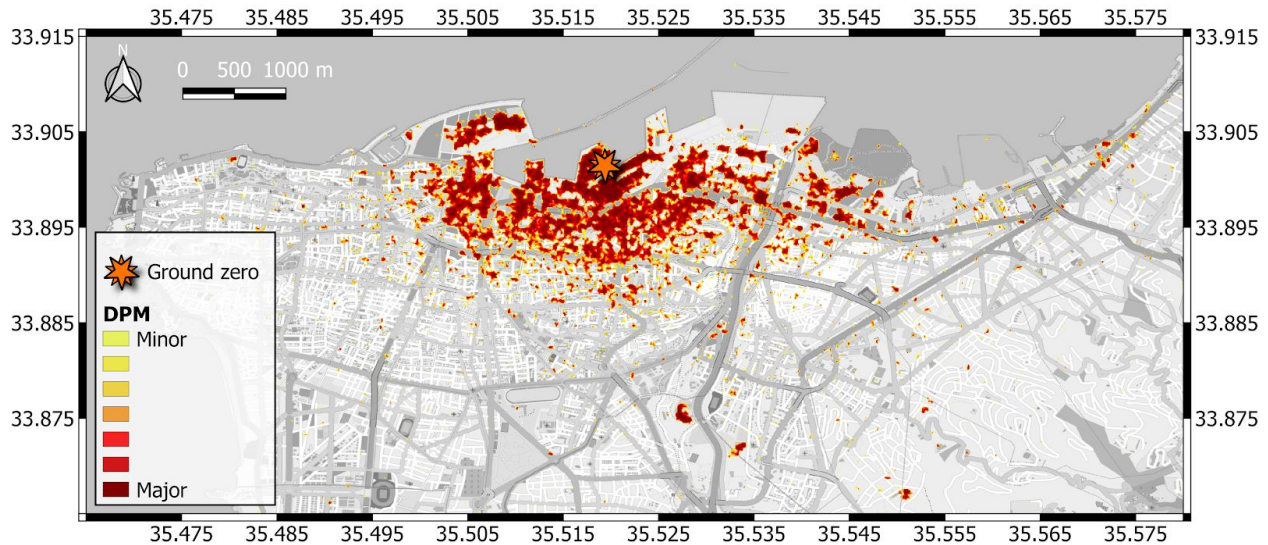


Figure 2.1. DPM produced following the 4 August, 2020 blast explosion.

2.3 Order of Engineers Damage Inspections

On August 12, 2020, the Beirut Order of Engineers and Architects (OEA) launched a large-scale field survey in the areas closest to and most affected by the blast, as illustrated in Figure 2.2. This effort was led by the OEA Public Safety Committee and utilized approximately one thousand volunteers of various specialties. A total of 3040 properties containing 2509 buildings were inspected in the designated area. The OEA also prepared reports (OEA, 2020) and a data bank that it intends to publicly release, and which in the interim has been made available for use in this study.

The OEA documented the condition of the buildings they surveyed, as illustrated in Figure 2.3, with special attention to heritage buildings, as shown in Figure 2.4. They also provided building-specific recommendations of evacuation, closure, or strengthening (full or partial, immediately or during works) to the most damaged buildings, as shown in Figure 2.5. Relative to ground zero, the OEA inspections occurred up to 1 km west, 1 km south, and 1.5 km east, in the districts of Minet El-Hosn, Zokak El Blat, Port, Saifi, Rmeil, and Medawar. At the southern limit of the inspection areas, damage levels of “no/minor damage” were recorded, whereas appreciable damage was observed at the western and eastern margins of the surveyed area, suggesting that additional damage locations beyond those limits may have been missed by the OEA surveys.

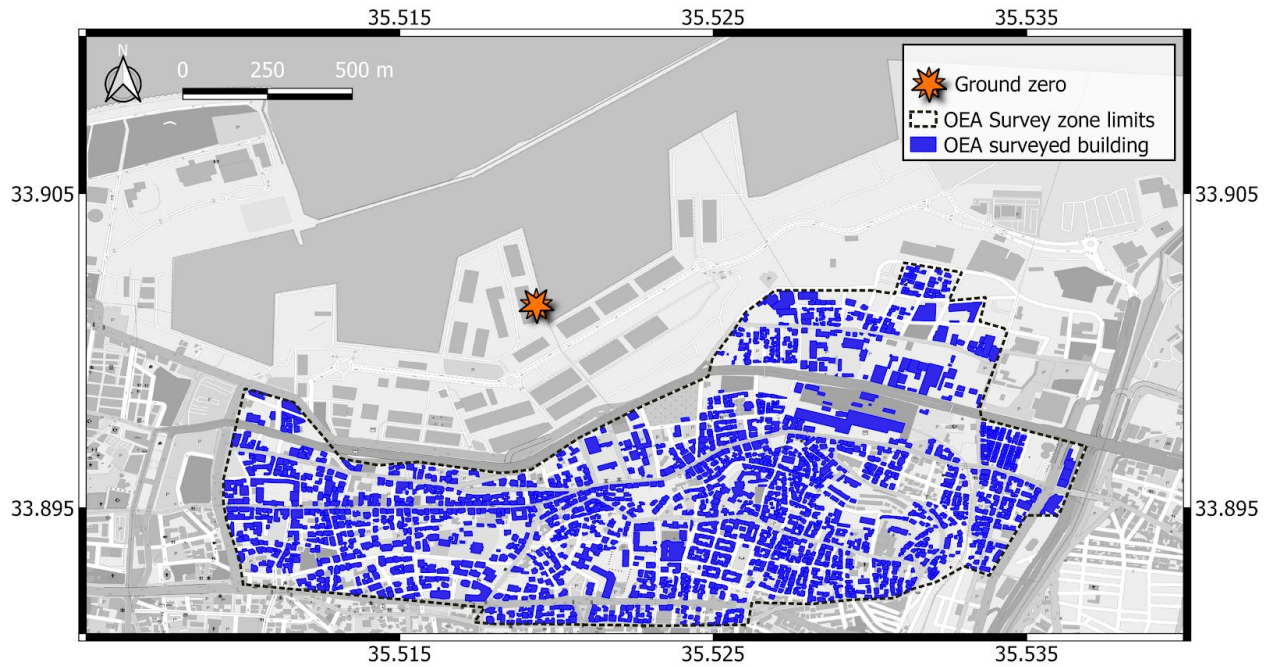


Figure 2.2 Locations of buildings in Beirut surveyed by OEA following August 4 2020 blast.

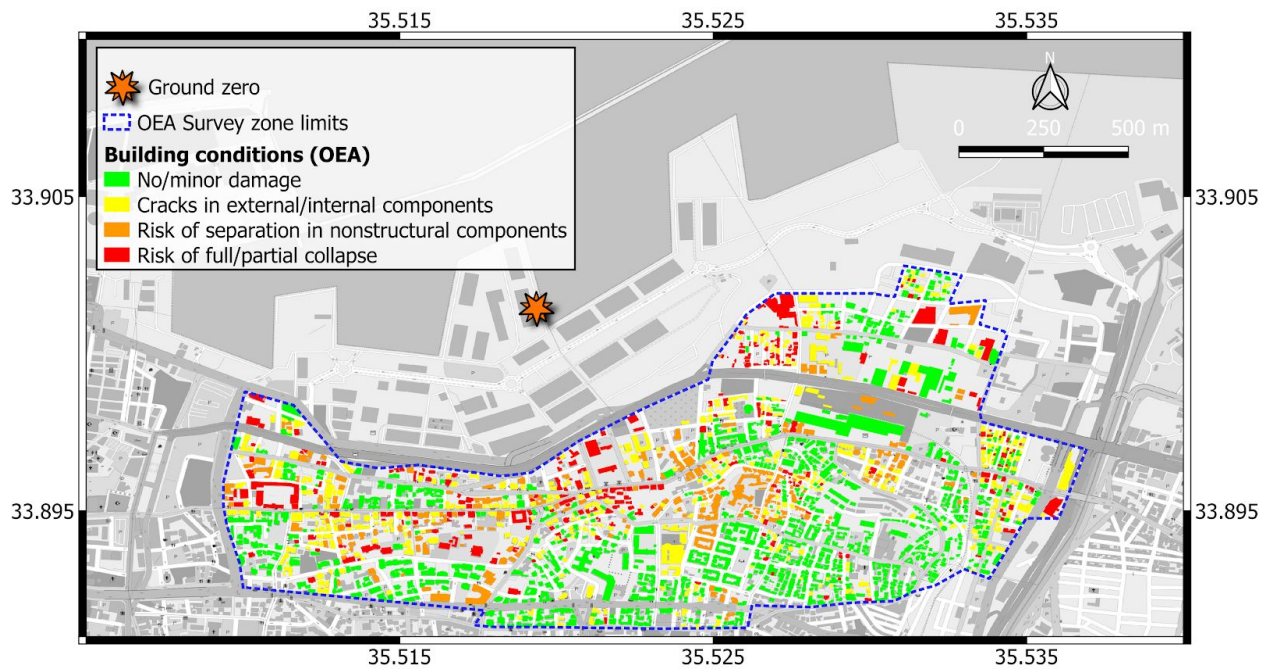


Figure 2.3 Conditions of buildings surveyed by OEA.

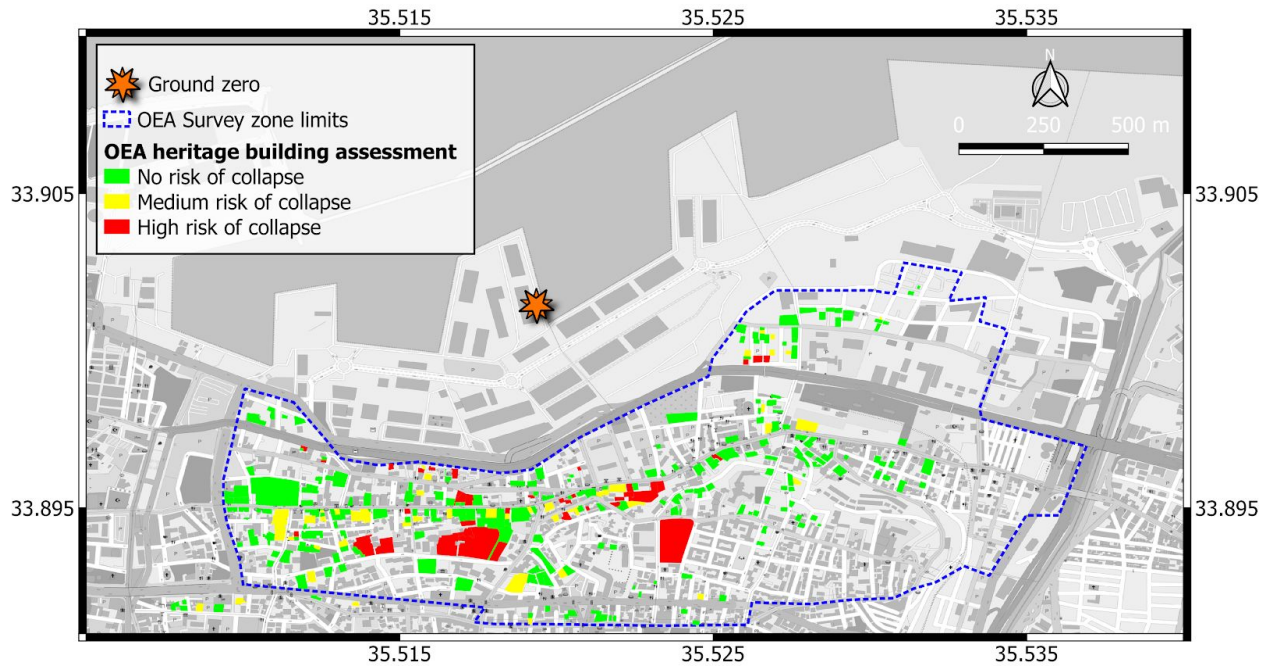


Figure 2.4. Conditions of heritage buildings surveyed by OEA.

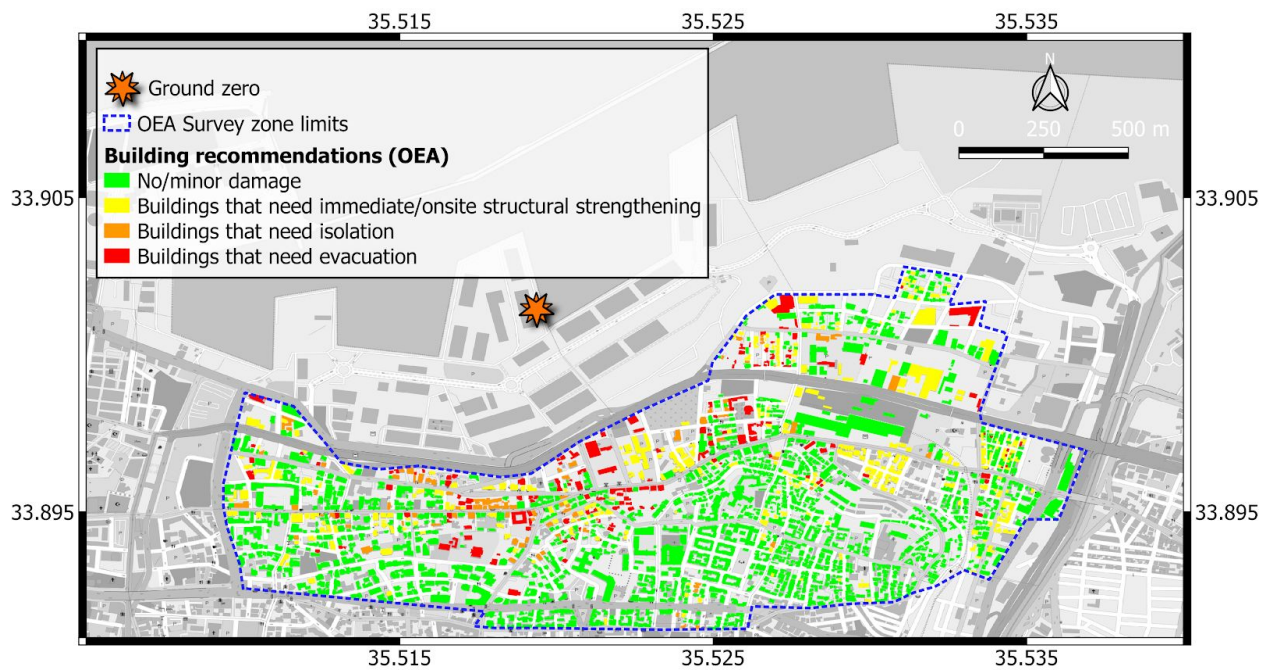


Figure 2.5 OEA recommendations on actions to be taken for surveyed buildings.

2.4 Open Map Lebanon

[Open Map Lebanon](#) is a community-based endeavor formed after the August 4 blast to promote data dissemination and relief efforts. One of the tasks undertaken by Open Map Lebanon is street-level imagery, which is compiled using Mapillary. A large fraction of the images available on the Open Map Lebanon Mapillary application were contributed by the present, GEER effort (details in Chapter 4).

Researchers at NASA-Jet Propulsion Lab (JPL) accessed these images to classify damage as “none,” “minor,” and “major” (Sang-Ho Yun, personal communication 2021). These assessments were not intended to provide information on building damage from engineering or building-use perspectives. Rather, they were intended as preliminary, general descriptions to facilitate visualization of relative damage levels across the city for comparison to DPMs. These assessments are not yet publicly available.

3.0 Impact on Port of Beirut

3.1 Description of Port Facility

Beirut is one of the oldest cities in the world, continuously inhabited for more than 5,000 years. The city coastline and safe water harbor/port(s) have shifted westwards and northwards over various periods of expansion and reclamation. The earlier Phoenician port and associated dry docks were identified in recent archeological exploration as being well within the current center of the Beirut central district (approximately 300m south of the current coastline). The Port of Beirut has seen periods of expansion and functionality change over the various eras. During the Roman presence (64 BC to the middle of the 6th century AD), it was developed into a commercial and economic center serving the “colonies”. This was followed by a succession of periods (Omayyad, Crusaders and Mameluke) in which the Port was the berth of armed fleets and later served as a hub for pilgrims visiting the holy lands.

The “modern” incarnation of the Beirut Port leading to its present extent started in the late 19th century when a concession was given by the Ottoman authorities to a private company to expand and manage the facility. Following World War I, under the [French Mandate for Syria and the Lebanon](#) (i.e., a period of French oversight of local governance), the Port management company was reorganized and granted a new concession in 1925 that ended in 1960. From 1960 to 1990 a Lebanese company operated the Port, after which it was returned to the state. Figure 3.1 shows the significant expansions of the Port facilities that were made since 1875, including the number and size of docks, deeper drafts, and larger commercial and storage areas.

In the past 30 years, further and more significant expansions of the port were completed. These allowed for a large container facility and larger and deeper water docks allowing the facility to receive the largest container/cargo vessels. As of 2019 the Beirut port accounted for more than 60% of Lebanon’s total imports (NY times, 2020) valued at roughly 25% of GDP.



Figure 3.1. Scaled representation of Beirut Port expansion from 1875 to 2020.

Figure 3.2 shows two early images (dating back to the late 19th century) showing the original expansion works at the port, which produced some of the present quays. These images

illustrate the nature of the earthworks/filling and quay wall types (apparently gravity concrete blocks, with possible dead-man anchors. In the modern expansion to the north, the quays consisted of cast-in-place concrete slabs supported on driven piles.



Figure 3.2. Works on the Beirut Port expansion in 1886. Note the cast large blocks, which would then be taken and sunk into position.

In the mid to late 1960s plans were drawn and executed to build the largest grain storage facilities of their kind in the region. Phase I of the project consists of 8 silo columns 3 rows deep. Phase II extended the facility to 14 silo columns 3 rows deep with a total capacity of 105,000 tons of grain, and was completed in 1969 (Figure 3.3). The Beirut Port Silos were considered a feat of engineering at the time. They consisted of 3 parallel rows of 14 cylindrical concrete silos, supported on 2900 driven precast reinforced concrete piles 12-15m deep. Phase III saw the addition of 6 additional cells raising the total number of rows to 16 and the capacity to 150,000 tons (Figure 3.4). Figures 3.5 to 3.8 show stages of the foundation work, along with a typical foundation plan/pile layout and an indicative subsurface profile. The soil profile in Figure 3.8 is part of project execution drawings and is based on data from borehole campaigns (data from 10 boring logs is summarized in Figure 3.8, but the original logs are not available as of this writing).



Figure 3.3. Phase I grain silos completed and Phase II nearing completion (adapted brochure Council for Large Projects-Lebanese Ministry of Public Works, 1970).

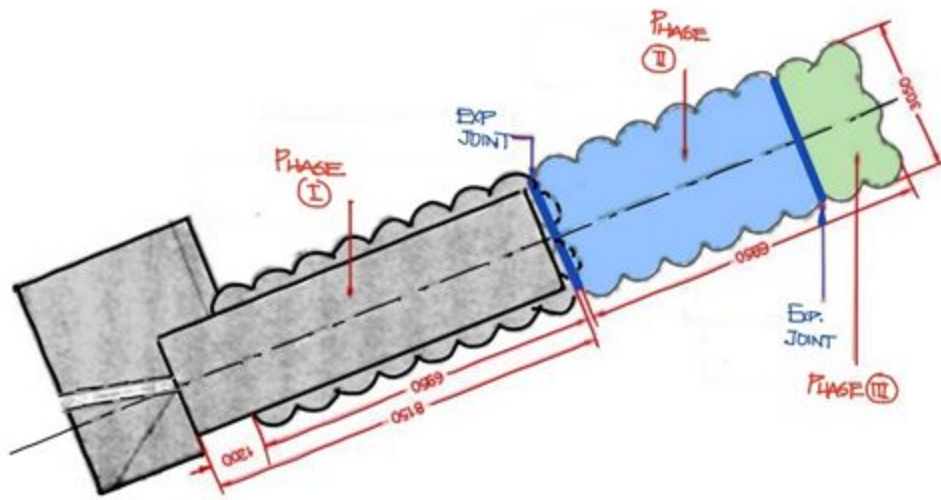


Figure 3.4. Plan view showing the grain silo complex with all three phases completed. Dimensions in the figure are in centimeters.

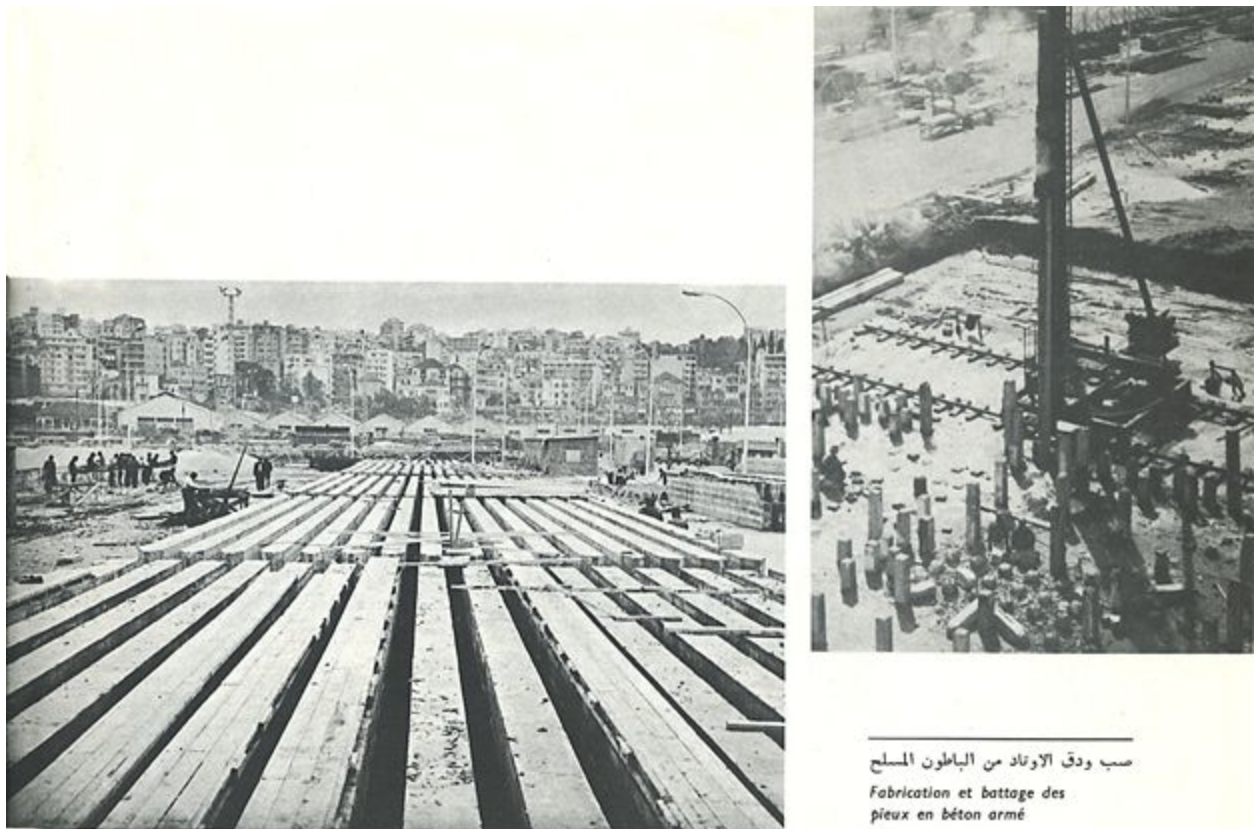


Figure 3.5. Grain silo foundation construction: Casting of 30x30 cm square reinforced concrete piles and pile driving (adapted from the High Council for Large Projects, Ministry of Public works, 1970).

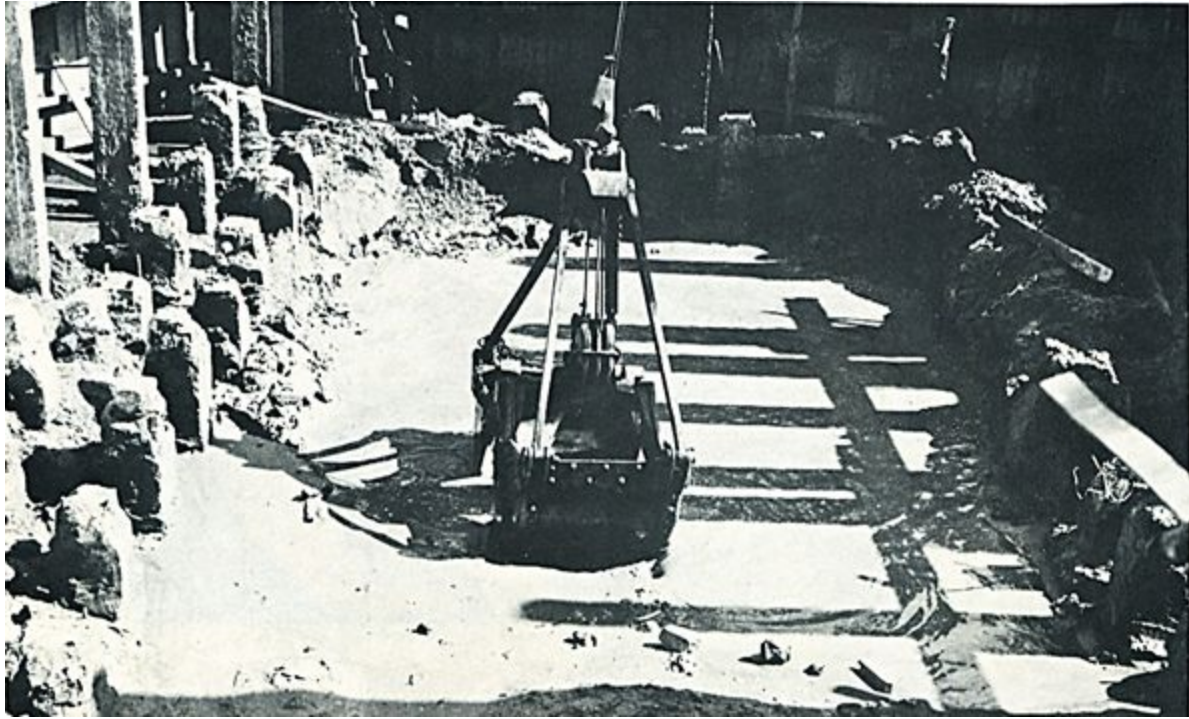


Figure 3.6. Excavation for the silos base slabs and exposing the pile heads prior to casting of the caps (adapted from the High Council for Large Projects, Ministry of Public works, 1970).

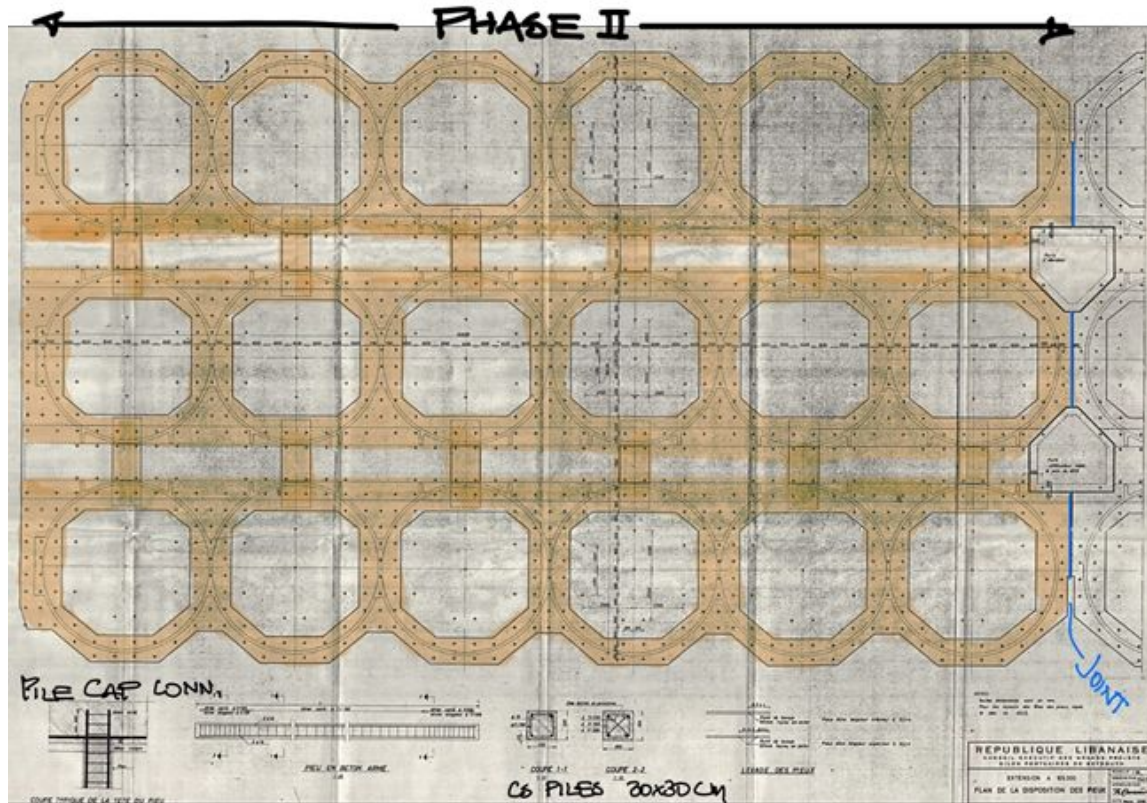


Figure 3.7. Copy of original foundation plans. The pile locations are marked by (+) on the map.

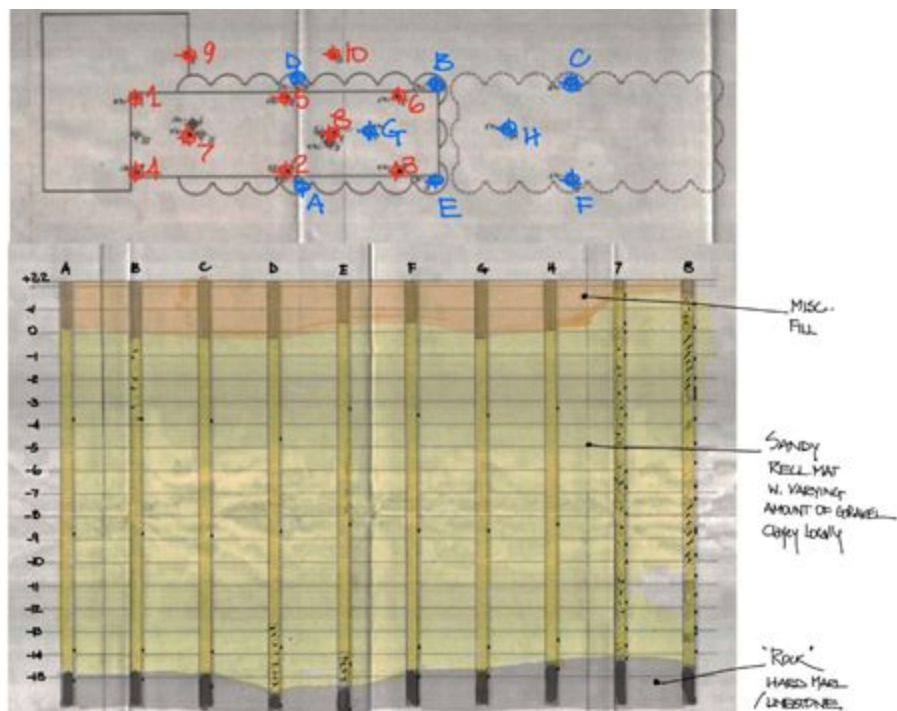


Figure 3.8. Only available Information re. the foundation materials in the Silos zone. Mostly fill of a predominantly sandy/silty nature.

In the late 1990s a comprehensive structural assessment was conducted on the silos. Significant deterioration of the 17-18 cm thick outer concrete silos shells was observed, mostly due to exposure to the humid and salty seafront environment and subsequent carbonation. The damage was addressed/mitigated by constructing a 12 cm thick reinforced concrete jacket onto the inner walls of the outer/exposed silos. This strengthening measure played a role in conditioning/improving their response to the blast on 4 August 2020. Figure 3.9 presents images taken in the aftermath of the explosion showing the process of coring through one of the western cells. The original concrete along with the 12 cm newly placed jacket can be clearly seen.



Figure 3.9. Coring through one of the “intact” cells. Note the improvised protection from falling debris from the damaged silo roof. The original concrete and the inner concrete jacket can be clearly seen in the recovered 30 cm core.

Figure 3.10 shows a map of the Port facility with its various basins and quays as it was before 4 August 2020. The silos and the various hangars are indicated. Note the location of Hangar 12 in which the ammonium nitrate was stored, in relation to the silos and the rest of the Port facilities.

Figure 3.11 shows the relevant basins and pre-explosion bathymetric levels (unverified). The levels shown on that figure were obtained from the port authority (personal communication,

2020) and provide a base reference that will be used to evaluate the material flow into Basin 3 as a result of the explosion.



Figure 3.10. Aerial view of Port of Beirut prior to 4 August 2020 explosion. Quays (numbers) of relevance are also shown for reference.

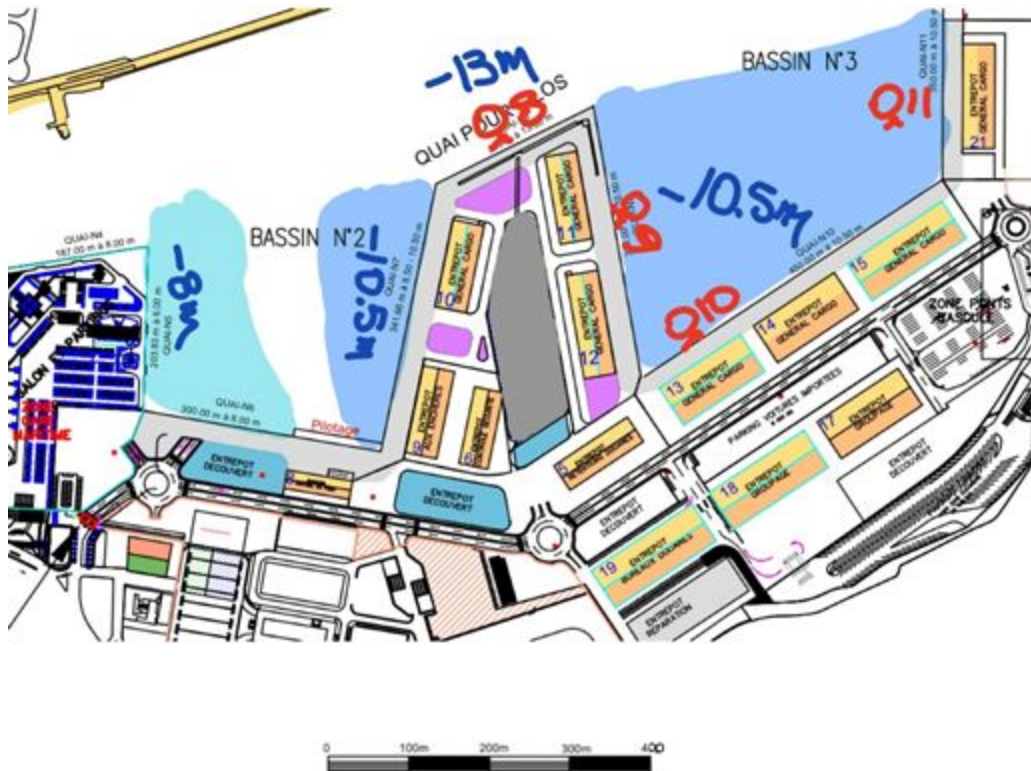


Figure 3.11. Basin 3 and associated quays. Pre-explosion bathymetric levels shown. The red text indicates quay numbers (e.g., Q10 = quay 10).

3.2 Explosion Impacts

As a result of the explosion, damage occurred throughout the Port facility. Steel-framed hangars were completely destroyed along with many small concrete and masonry structures. All the storage yards and loading docks were damaged by the blast and all goods, materials, and infrastructure present in those areas were unrecognizable and/or damaged beyond repair. Luckily for Lebanon, the northernmost parts of the Port, namely the new container terminal, were largely spared the devastating effect of the blast, allowing limited Port operations to continue.

This chapter describes the impacts of the explosion within the Port, including areas with severe and relatively limited effects. The zones of particular interest covered in this chapter include:

- The silos and adjacent areas
- Hangar 12. Specifically, the crater and debris displaced from that location
- Any discernible ground movements and/or deformations across the port, including portions of the Port with limited damage that remained in operation.

3.2.1 Grain Silos

When combined together, the Beirut Port grain silos comprise a substantial structure, roughly 175m long and 30m wide, with a height of 50m. Parts of the silos were full or partially full with grain at the time of the event, thus increasing their mass and the bulk resistance of the thin concrete shell cylinders. Figure 3.12 shows a plan view of the facility (Google Earth-Satellite image) shortly before the event.



Figure 3.12. Plan view of the silos and Hangar 12 in June 2020 (from Google Earth). There are 16 columns and 3 rows of silos.

Figures 3.13-3.21 show the extensive damage to the silos from the explosion, which was only 50 m away. Figures 3.13-3.15 show a photograph, diagram, and 3D point cloud from a LiDAR scan of the silos in plan (images from the LiDAR scans were provided by Mr. Emanuel Durand, personal communication, 2020). The point cloud data collected will be made publicly available once further analyses currently underway at the Universite Saint Joseph (USJ) School of Engineering are completed. An interesting web-accessible [3D rendering](#) (Bandera, 2021) of the silos based on LiDAR and photogrammetry reconstruction has been produced from the LiDAR data and drone imaging conducted by the Lebanese ministry of commerce.

The first (eastern-most) row of silos was completely destroyed by the blast, and is only visible as outlines of the base of the silos near ground level (and surrounded by spilled grain). The second row is mostly destroyed, and the third row (western-most) is mainly intact. The explosion exposed the gap at the construction joint between the Phase I and Phase II silos, as shown in Figure 3.13. There is no evidence of the gap having widened as a result of the blast. As shown in Figure 3.14, most cells were partially filled at the time of the explosion, except the

two rows at the south end. Interestingly, the third-row cells that survived were partially filled, whereas those that were lost (at south end) were empty.

Figures 3.16-3.20 are ground-level photographs of the damage to the silo structures. Figures 3.16 to 3.19 show the silo complex from various perspectives on the eastern side (nearest the blast). These images show the impact of the explosion on the shell structures and the spilled grain, which sits next to the shattered silos at its angle of repose. Figure 3.20 shows the silos from the western side, where they are mainly intact except for the lost silos at the south end of the series. The joint between Phase I and Phase II silos is clearly exposed.



Figure 3.13. Image taken from a drone looking towards the west. The red box shows the interface between Phases I and II of the silo construction, where the construction gap was revealed by the damage.

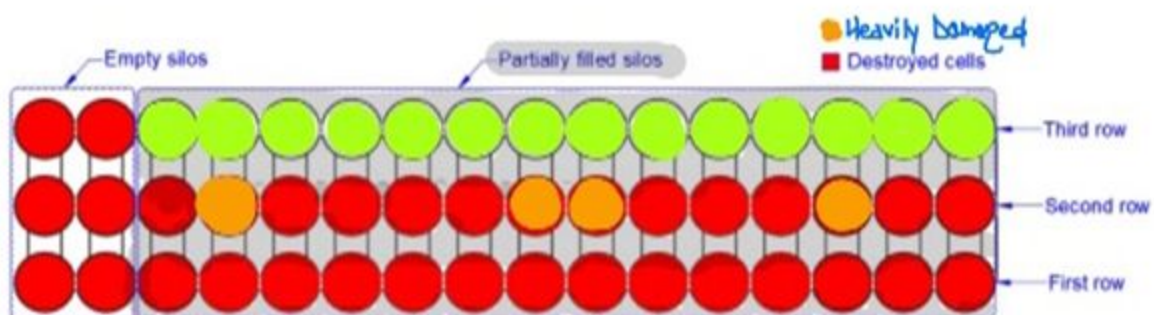


Figure 3.14. Schematic of damage levels observed on site. The top of the figure represents the western-cells furthest from the blast point.

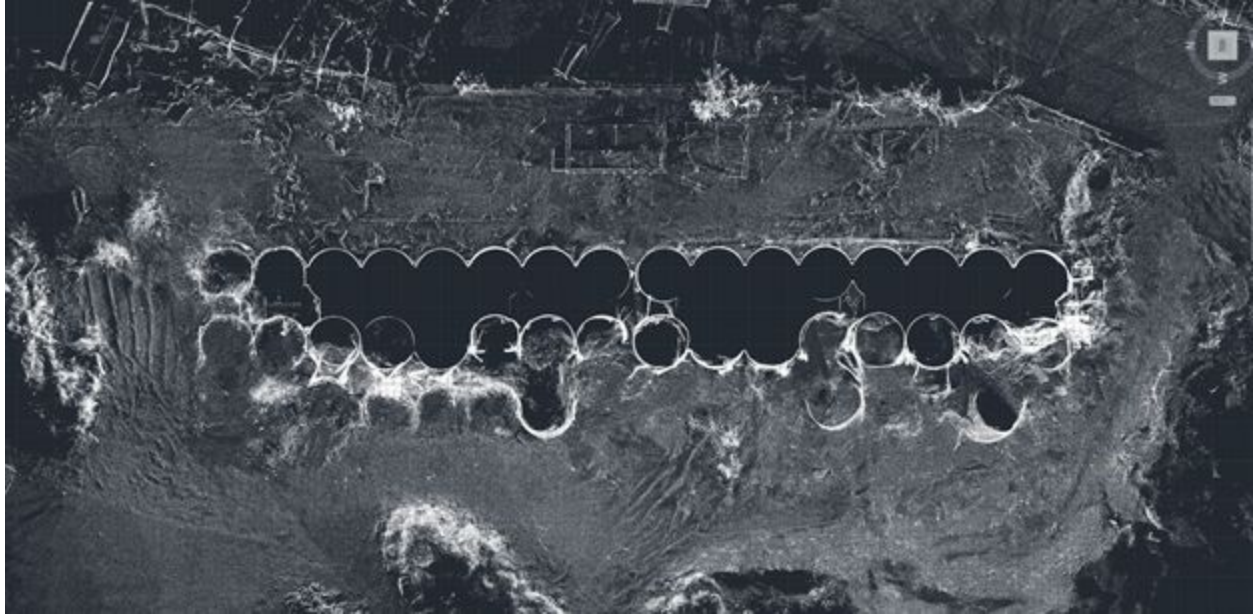


Figure 3.15. Processed image from drone-mounted LiDAR scan. The 3D point cloud is viewed from above (courtesy Mr. Emanuel Durand-Amann Engineering).



Figure 3.16. Frontal view of silos looking towards the west. Picture taken from Quay 10. ($33^{\circ}54'6.35''\text{N}$; $35^{\circ}31'16.19''\text{E}$).



Figure 3.17. Close-up view of the destroyed and severely damaged silos that were empty at the time of the 4 August 2020 explosion (33°54'0.51"N; 35°31'7.35"E).



Figure 3.18. Picture taken from the seaside close to Quay 8 looking south towards the city ($33^{\circ}54'6.97''\text{N}$; $35^{\circ}31'6.54''\text{E}$) . Note the mounds of grain (corn in this case) potentially contributing to structure stability.



Figure 3.19. Complete failure/crushing of the concrete and collapse of the shell structures ($33^{\circ}54'6.61''\text{N}$; $35^{\circ}31'5.43''\text{E}$).



Figure 3.20. View of the third row of silos (of Phases I and II) on the opposite side of the explosion source. The location of the last two columns of silos (Phase III) is shaded in the image; those silos are completely destroyed and not visible in the picture. (33°54'5.31"N; 35°31'3.38"E).

Figure 3.21 shows relative horizontal displacements of the third-row (western-most) silo as measured from LiDAR point cloud data with respect to ideally vertical cylinders of constant diameter. Negative displacement values are away from the blast, while positive ones are towards it. The relative horizontal displacements are measured as ranging from -0.24 to +0.28m. These data can be used to estimate the westward horizontal tilt of the third-row silos from the blast. By taking the relative horizontal displacements in the westerly direction at the top of the silos relative to the bottom (approximately 0.24 m), and dividing by the silo above-ground heights of 50 m, about 0.5% tilt is computed (0.3°). More detailed analyses of the deformations and base movements of the silos are underway at the USJ School of Engineering.

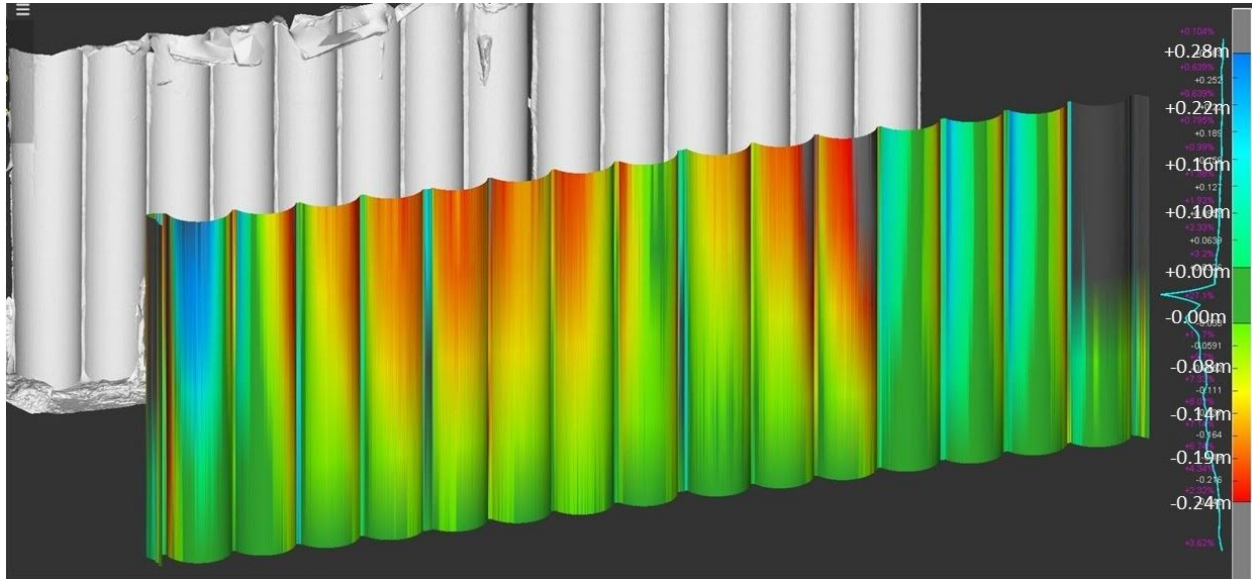


Figure 3.21. Horizontal deflections of west side of silos as evaluated from Lidar point cloud data. The amount of horizontal deflection is shaded as indicated by the scale bar (c. Mr. Durand). They indicate a consistent tilt at the top of multiple silos of around 24cm, all pointing away from the blast (view from the West looking East).

3.2.2 Ground Zero Crater

One of the most compelling features revealed by reconnaissance following the explosion is the almost 120m diameter crater left at the location of the blast source. This, along with the remnants of the silos have come to symbolize the intensity and ferocity of the energy released. Figure 3.22 includes before and after aerial view images of Hangar 12 and the crater.



Figure 3.22. Aerial views of ground zero (Hangar 12) prior to (31 July 2020) and immediately following (4 August 2020) the explosion (Google Earth).

In Figure 3.23, we superimpose the before and after images to provide a clearer view of the extent of the crater and related damage to docked vessels. Some of these vessels capsized, whereas a lighter ship was carried across Basin 3 and made landfall on an adjacent dock.



Figure 3.23. Superimposed Google Earth (™) images from 31 July 2020 and 5 August 2020. Straight arrow on the east side of Basin 3 shows the location of a capsized vessel (the Orient Queen). Curved arrow shows the before- and after-blast positions of a vessel washed up onto Quay 10 by the blast.

In the aftermath of the event, detailed bathymetric surveys were conducted by teams from the Lebanese and French armies using boat-mounted bottom profilers. The results of those surveys are presented for the area of concern in Figure 3.24. Figures 3.25 and 3.26 provide contour-based and isometric surface representations of the data in the areas near the quay wall. The 3D isometric surface rendering in Figure 3.26 provides a clearer view of the crater and earth movement as the original quay-wall was displaced/failed by the force of the blast. The localized high points visible in this rendering are artifacts of the interpolation.

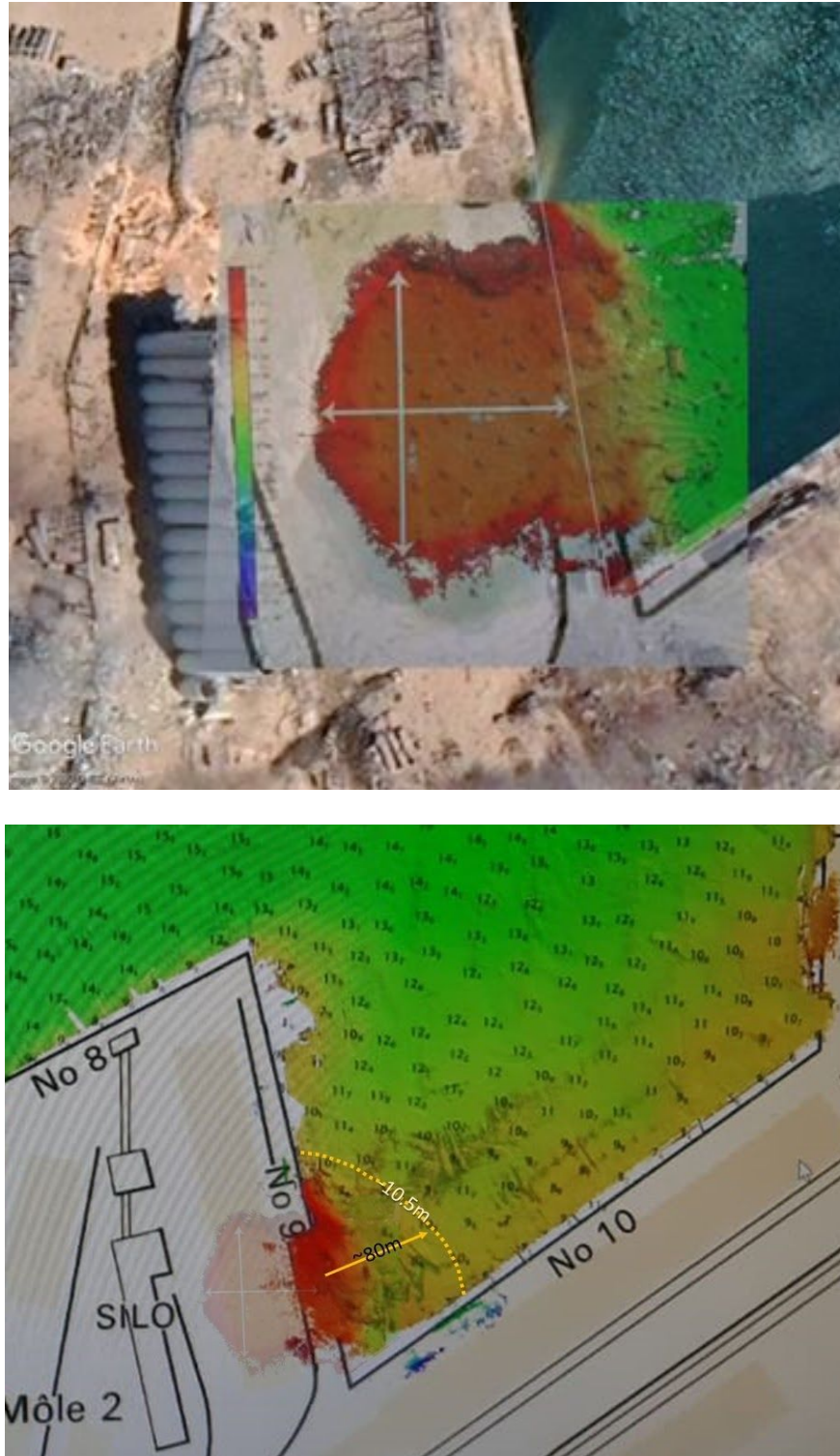


Figure 3.24. Top: Superposition of bathymetry survey on Google Earth image of crater and adjacent area; Bottom: Water depths from bathymetric survey and approximate limit of depth decrease from flow slide. Data from the Lebanese Ministry of Commerce.

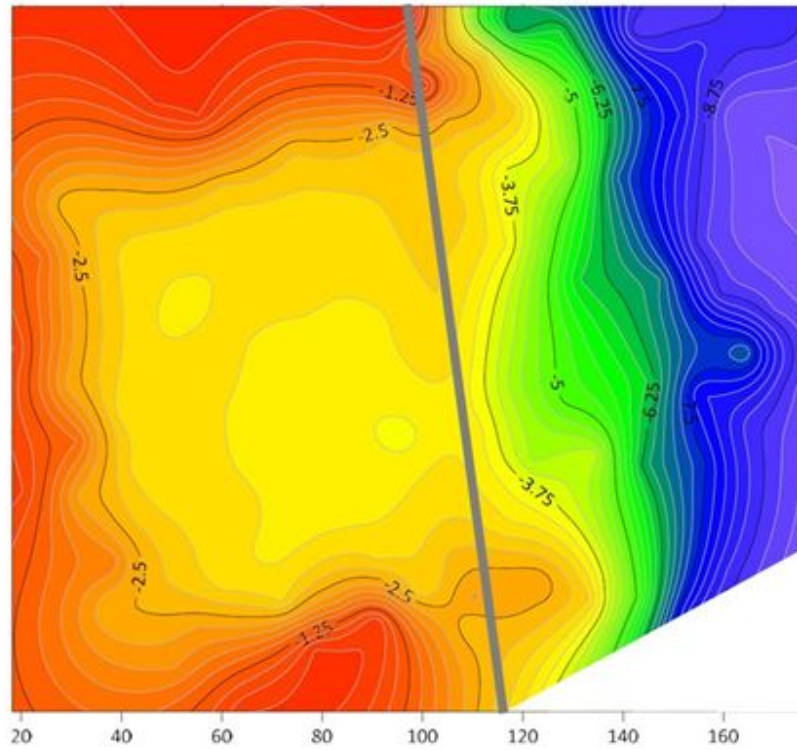


Figure 3.25. Depth contours (in meters relative to MSL) in the crater area. Gray line indicates the location of the former quay wall.

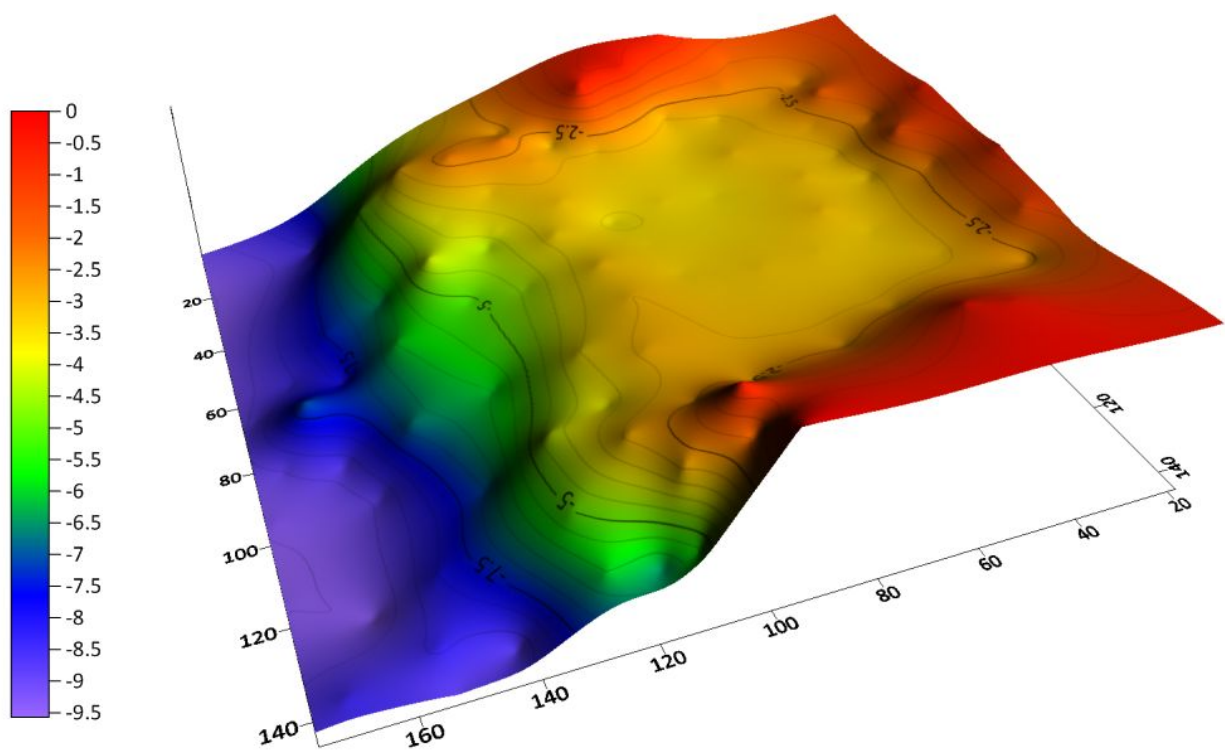


Figure 3.26. Isometric view of surface revealed by bathymetric survey. All units are meters.

Recalling that the originally reported bathymetric level for this part of the Port was approximately -10.5m (Figure 3.11), the extent of the significant flow of materials beyond the original position of the quay wall becomes clear. The depth of the crater (including original ground level taken as approximately +1.5m and the part reflected in the bathymetric contours below the waterline) can be estimated to have a maximum value of 4 to 5m. The resulting Depth to Diameter Ratio (DDR) would then be approximately 0.04, which is below the lower range of typical measured DDR for large blasts (>100 tons of TNT equivalent). The somewhat shallower impact depth in the Beirut Port event could be attributed to the high water level (only 1.5m below surface), and the lateral release/flow of some of the material into the adjacent deeper basin.

If we consider a pre- and post-explosion section along the center of the crater, it may be represented by the schematic shown in Figure 3.27. This conceptual rendering shows how we can use the data from the bathymetric contours and the original ground surface level to calculate volumes of soil displaced from behind the wall (volumes II and III) and accumulated below the wall within the original basin (volume I).

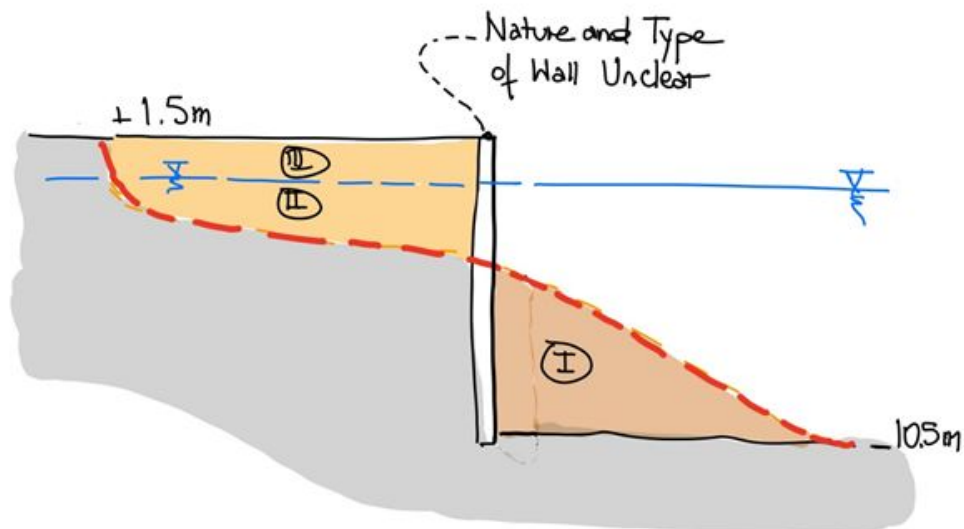


Figure 3.27. Schematic of a pre and post event section through the crater.

This analysis was done using the software packages Mathematica[®] and Solidworks[®]. The shapes of the volumes as rendered in the analyses are shown in Figure 3.28. The following results were obtained:

- Volume I: Material displaced into the basin $\sim 38,500 \text{ m}^3$
- Volume II: Below-water material “lost” from behind the original quay wall $\sim 29,500 \text{ m}^3$
- Volume III: Above-water material “lost” from behind the original quay wall $\sim 16,000 \text{ m}^3$

The balance of the material on either side of the quay wall is $(v\text{-II}+v\text{-III}) - v\text{-I} \sim 7000\text{m}^3$. This “unaccounted” for soil was probably thrown up into the air for longer distances in various directions by the blast (mostly the above water level fill) and/or due to the many simplifying assumptions we made in the analysis, including all uncertainties related to the original system and levels, etc. Nonetheless, these numbers confirm the likelihood of a flow of the retained fill as the quay-wall structure was “lost”/failed due to the blast. The material apparently flowed up to a maximum distance of approximately 60 to 80m as can be seen from Figures 3.24. As such, the data could be used in a back-calculation of residual strength.

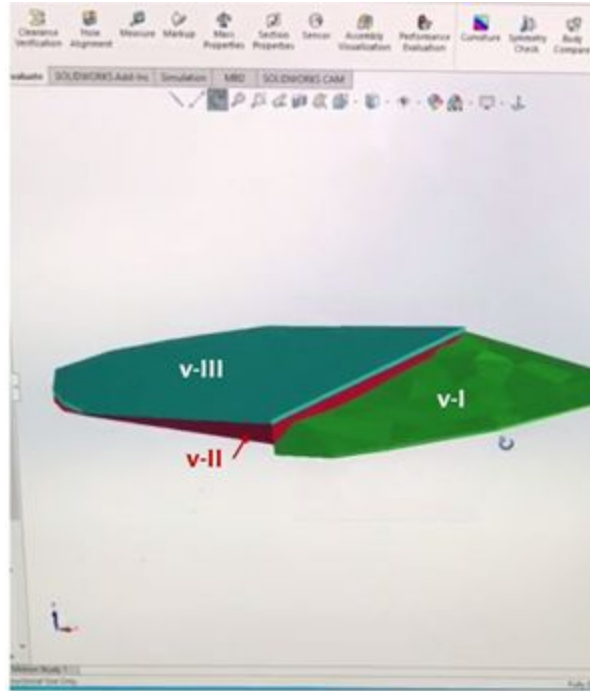


Figure 3.28. Screen shot from Solidworks software showing the 3D volumes analyzed.

3.2.3 *Other Ground Movements and Observations Across Port Complex*

Evidence of ground movement could be seen across the central and western parts of the Port, particularly for locations closer to ground zero. We performed field inspections of the Port complex 6 weeks following the explosion.

At the time we visited the site, much of the scene had been significantly changed and modified by the rescue and emergency removal operations. Nevertheless, it still was possible to note some surface deformations, loss of material via possible internal erosion or water overtopping and eroding unpaved parts of the docks. These observations are presented and commented upon in Figures 3.29 to 3.37.



Figure 3.29. Reference map for the observations and pictures included in this section.



Figure 3.30. Ground deformation and mini-cratering exposed by truck traffic and possible resulting from loosening and/or shifting of the fill below. (33°54'0.86"N; 35°31'9.30"E).



Figure 3.31. Surface expressions similar to Figure 3.30 at a location close-by. ($33^{\circ}54'1.09''\text{N}$; $35^{\circ}31'7.59''\text{E}$).



Figure 3.32. Dock along Quay 10. This location was paved. The expression of the ground deformation below the surface was exposed as a result of heavy earth moving equipment. Note the overall downwards settlement from the presumed original quay level ($33^{\circ}54'2.00''\text{N}$; $35^{\circ}31'11.36''\text{E}$).



Figure 3.33. Close-up of the void below the asphalted section/pavement (33°54'2.00"N; 35°31'11.36"E).



Figure 3.34. Medium-size vessel that was docked at Quay 9, lifted by the water wave generated by the explosion and left on the dock at Quay 10.(33°54'3.04"N; 35°31'11.94"E).



Figure 3.35. Closer view of the vessel with evidence of the indentation caused by the pressure wave. (33°54'4.13"N; 35°31'12.74"E).

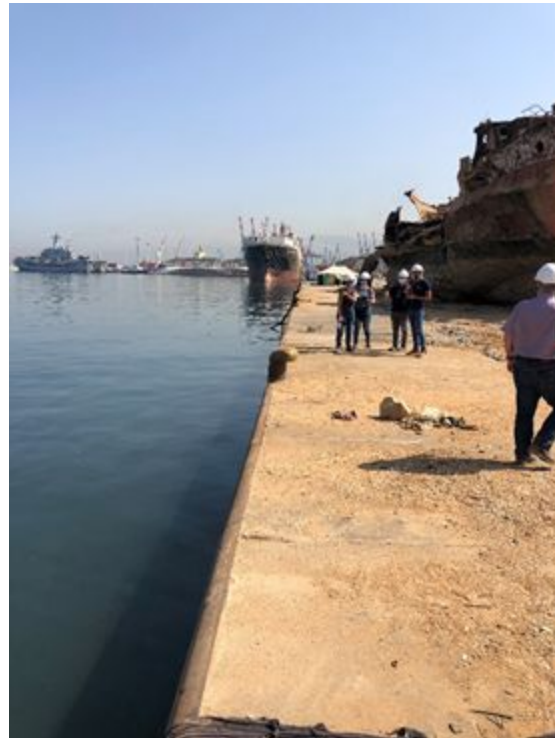


Figure 3.36. No evidence of damage to the western section of Quay 10. Alignment and level of the top quay slab in this section is intact (Location of these images is indicated by the red lines on Figure 3.29) (33°54'4.23"N; 35°31'15.04"E).



Figure 3.37. Typical damage done to steel structures throughout the Port. All suffered either this level of damage or worse (extent evident in Figure 3.29) (33°54'4.23"N 35°31'15.04"E).

As noted previously, the Port of Beirut was not completely out of service following the 4 August 2020 explosion. In particular, quays to the south and east of Basin 4 (locations shown in Figure 3.10) and the Container Terminal remained operational. These areas are further from the blast source (approximately 1200m) than the quays bounding Basin 3. However, the standards of construction in this part of the Port were also higher, being part of the post-1950 Port expansion. The quay slabs were built on driven large diameter steel piles, as shown in Figure 3.38. Permanent ground deformations were not observed in this area and the cranes remained operational with no distortion to their tracks.



Figure 3.38. Piles driving in Container Terminal portion of Port of Beirut as part of 2011 expansion.

4.0 Impacts on Buildings

The City of Beirut has a rich architectural history and contains building structures spanning many construction eras. Structures built before the 1950s-60s typically consist of low-rise stone masonry bearing wall buildings developed without adherence to modern building codes. Several of these structures that have architectural or historical value are classified as *heritage* buildings by the Ministry of Culture Directorate General of Antiquities (DGA). Mid-rise reinforced concrete frame structures emerged in the 1950s. Then, during the Lebanese civil war (1975-1990), building construction was affected by poor building code design provisions and lack of material quality control (Salameh et al. 2016). Despite being an area of moderate seismicity, during that era most of the buildings in Beirut were designed to resist gravity loads only, with little or no consideration to lateral resistance. Seismic provisions in building codes were introduced in the 1990's, and although not strictly enforced until 2013 (with the publication of the second edition of the Lebanese earthquake standards; Libnor, 2013), structures built after 1990 can generally be considered as modern structures. Table 4.1 summarizes the evolution of the building stock in Beirut with time, namely, the typical structural systems, the design and construction quality, and the building heights.

Table 4.1. Characteristics of the Beirut building stock (adapted from Salameh et al. 2016).

Year	Structural System	Likely Design and Construction Quality ²	Height
Before 1935	stone masonry bearing walls ¹	GLD - Good	Low-rise
1935-1955	stone masonry bearing walls ¹	GLD - Good	Low-rise
	mixed stone masonry bearing walls and reinforced concrete frame	GLD - Good	Low-rise; Mid-rise
1955-1975	reinforced concrete frames	GLD - Good	Mid-rise
1975-1990	reinforced concrete frames	GLD - Poor	Mid-rise
1990-2005	reinforced concrete frames and walls	GLD or SD - Good	Mid-rise; High-rise
After 2005	reinforced concrete frames and walls	SD - Good	Mid-rise; High-rise

¹Slabs are either wooden, reinforced concrete, or steel

² GLD = gravity-load design; SD = seismic design

This chapter describes the efforts undertaken to document the performance of the Beirut building stock to the 4 August 2020 explosion. Sections 4.1 and 4.2 describe the data collection efforts, which consisted of in-person building inspections conducted shortly after the blast and street-view imagery collected two month after the blast. Our efforts to collect this data were strongly affected by the global COVID-19 pandemic, which prohibited international travel, as well as US-Lebanon shipping restrictions, which limited our ability to import reconnaissance equipment (e.g., from the NSF-sponsored [RAPID site](#)) to assist in the work. Sections 4.3 and 4.4 present our interpretation of the data in terms of structural performance and facade damage, respectively. Section 4.5 describes the correlation of the observed damage indices with DPMs (introduced in Section 2.2).

4.1 In-Person Building Inspections

The Maroun Semaan Faculty of Engineering and Architecture (MSFEA) at the American University of Beirut set up an emergency hotline and engineering dispatch center for Beirut residents and businesses concerned about the structural safety of their buildings following the Beirut Port explosion. Teams of engineers led by faculty members from MSFEA were on call for four weeks, between August 7 and September 4. MSFEA faculty members, lecturers and lab managers led the teams, and current graduate and undergraduate students or alumni assisted them with data collection and documentation. The teams visually assessed buildings and provided advice on the possibility of imminent danger stemming from structural, non-structural, or falling hazards, and recommended possible mitigation measures. Some of the faculty coordinating this effort within AUB are members of the GEER team and the collective findings are presented and used in this report.

As phone calls were received from building owners or tenants on the emergency hotline, visits were scheduled with the callers, and a team was dispatched. Each visit started by a visual assessment of the exterior of the structure, followed by the evaluation of the interior of the building in part or in full whenever possible. The team photographed the building façade(s) and structural &/or non-structural damage visible inside or outside of the building. They completed an assessment survey form for each structure visited. In general, visits lasted between 15 and 45 minutes per building. At the end of a visit, the owner or tenant was provided with advice and recommendations for further action, if any was needed (e.g., retrofit, secure, or scaffold).

The assessment form was based on the ATC-20 (1995) and ATC-45 (2004) rapid and detailed evaluation safety assessment forms, with modifications to suit the local setting. The form included information about the building itself (age, dimensions, type(s) of occupancy, type(s) of structural system) and observations of damage to the structure (App A). An important distinction between these building inspections and those by OEA (Section 2.3) is that the structural observations more specifically delineated damage to structural (i.e., load-bearing) vs non-structural elements, which conforms with protocols widely used in post-earthquake

reconnaissance. Some of the damage recorded in these surveys may have preceded the explosion (e.g., shrapnel during the Lebanese civil war, prior settlement of foundations, corrosion due to water leakage...), but were still reported in the survey forms. They were distinguished from damage due to the explosion whenever possible through visual identification or when reported as such by the tenants.

The survey form was first implemented on Fulcrum (14-day free trial version) <https://www.fulcrumapp.com/>, between August 7 and 14. In the meantime, a version of the survey was developed on ArcGIS Survey123 (ESRI), for which AUB already held licenses (see Figures A.1-A.3). The assessment forms between August 14 and September 4 were completed on ArcGIS Survey123. In both cases, the survey forms were filled electronically through their respective mobile applications.

A total of 172 buildings were inspected during this effort. The locations of these buildings are shown in Figure 4.1. Most of them are located within 2 km from the blast. The buildings were classified into one of three damage categories, adapted from ATC-20 (1995) and ATC-45 (2004) rapid and detailed evaluation safety assessment forms to suit the local setting: safe (green), restricted use (yellow), and unsafe (red). A more detailed description of these categories is provided in Table 4.2.

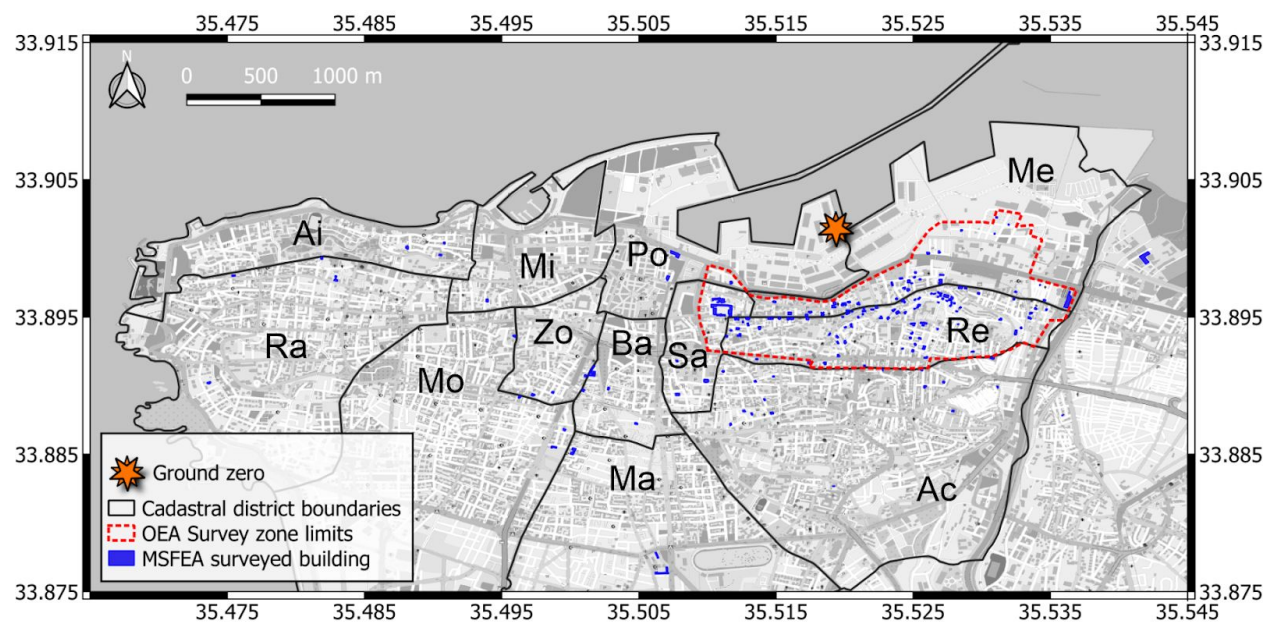


Figure 4.1. Buildings inspected by MSFEA as part of the GEER reconnaissance.

Table 4.2. Building safety classification applied during MSFEA building inspections. Adapted from ATC-20 (1995) and ATC-45 (2004).

Inspected/Safe (Green)	Habitable, minor or no damage No apparent hazard is found, although repairs may be required. The original structural integrity is not significantly decreased. No restriction on use or occupancy. Damages in these buildings are mostly limited to glazing, doors, cladding, false ceilings or minor to moderate cracks in partition or infill walls.
Restricted Use (Yellow)	Damage which represents some degree of threat to occupants A hazardous condition exists (or is believed to exist) that requires restrictions on the occupancy or use of the structure. Entry and use are restricted until the owner can hire an engineer or architect to develop the necessary repair program. These correspond to buildings that have sustained some structural damage or significant non-structural damage or may be subjected to non-structural hazards (e.g., potential failures of partition walls or falling of roof brick elements).
Unsafe (Red)	Not habitable, significant threat to life safety Extreme structural or other hazard is present. There may be imminent risk of further damage or collapse, which represents a threat to the life safety of persons occupying these buildings. These buildings are thus unsafe for occupancy or entry. These correspond to buildings that sustained major structural damage and are at risk of partial or complete collapse. It is important to note that this category does not mean that the facility so tagged must be demolished, it simply means that the facility is not safe enough to occupy. In the vast majority of cases, structures posted unsafe can be repaired to a safe and usable condition with proper measures to be taken immediately.

4.2 Street-View Photo Survey

Street-view high-resolution photograph surveys were performed on 8 and 15 October 2020. The purpose of these surveys was to document the damaging effects of the blast for a large number of structures, albeit with much less information per structure than the in-person inspections provide.

We originally attempted to utilize street-view equipment owned and maintained by the NSF-sponsored [RAPID site](#). Considerable effort was invested in seeking ways to transport the equipment to Beirut either by hand-carry from a GEER team member (abandoned because of COVID-related travel difficulties) or shipping the equipment from Seattle, Washington to Beirut. These were ultimately deemed unworkable, and as a result, we used commercially-available GoPro equipment (GoPro Fusion). These difficulties produced delays in the street-view imaging that was ultimately undertaken, which explains the two-month time lag between the event and the completion of the survey.

The GoPro Fusion camera was mounted to the roof of a car. The camera was used in a mode that allows manual control on the number of images taken in order to ensure an optimal coverage with a practical number of images. All photos are geo-tagged (i.e., the location of the camera is recorded as a latitude/longitude) and the azimuth of the photograph (i.e., the direction that the camera is pointed towards) is recorded. Figure 4.2 shows the route taken by the camera-mounted car. Note that this method of reconnaissance could be undertaken safely given the public health challenges that were present at that time in Beirut. Figure 4.3 shows example images from the survey. All of the images (2100 in total-shown as individual dots on Fig. 4.2) and the related metadata collected in this survey, were uploaded to [mapillary.com](#) (username: aubmsfea).

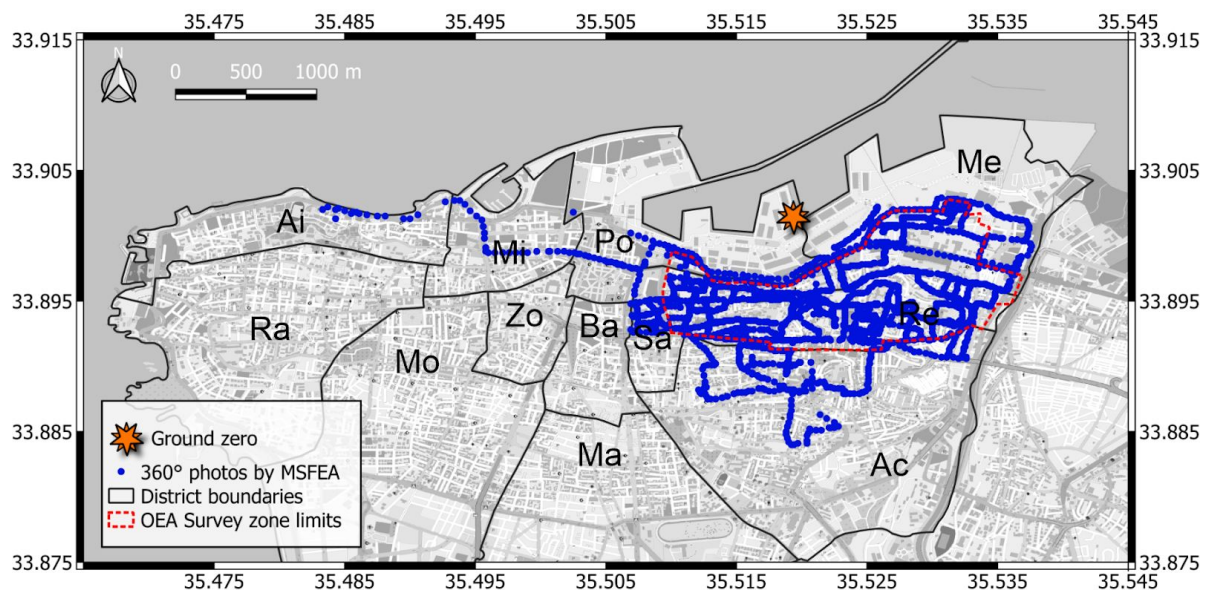


Figure 4.2. Tracklog of street-view photo survey undertaken on 8 and 15 October 2020.



Figure 4.3. Example images from street-view photo survey as captured (left) and as viewed using the GoPro VR player (right): (a) 33.8951° N, 35.5097° E, approximately 90° azimuth (right); (b) 33.8945° N, 35.5114° E, approximately 90° azimuth (right).

4.3 Structural Damage Assessment

4.3.1 Damage Re-Classification

For the purpose of this report, the visually assessed buildings (Section 4.1) were re-classified according to a system adapted from Bray and Stewart (2000) and EMS98 (Grünthal, 1998). The system consists of assigning to each building a damage index between D0 (no observed damage) and D5 (complete collapse of a floor or the entire structure). The description of these indices, and our field interpretation of them in the context of Beirut, is presented in Table 4.3.

Table 4.3. Structural damage classifications*. Adapted from Bray & Stewart (2000) & EMS98 (Grünthal, 1998).

Structural Elements	Damage Summary	DAMAGE DESCRIPTORS BY TYPOLOGY	
		SANDSTONE BEARING WALL BUILDINGS	RC BUILDINGS
D0	No Damage		
D1	Light Damage		
Load-bearing structural elements	No damage	Hairline cracks in a few walls Fall of small pieces of plaster only	Fine cracks in plaster over frame elements or in wall bases
Non-structural elements**	Minor damage/cracking		Fine cracks in partition and infill walls
D2	Moderate Damage		
Load bearing structural elements	Minor damage / cracks (insignificant displ. across cracks)	Cracks in many walls Fall of large pieces of plaster	Cracks in columns, beams and structural walls.
Non-structural elements	Moderate damage/cracking.	Moderate damage to façade arches or balconies Moderate damage to roof or ceilings	Moderate cracks in partition and infill walls Fall of brittle cladding and plaster. Falling mortar from the joints of wall panels. Moderate to heavy damage of false ceilings.

D3		Heavy Damage	
Load bearing structural elements	Significant damage (cracking with significant deformations across the cracks), but no collapse	Large and extensive cracks in most walls Tilting or separation of bearing walls	Cracks in columns and beam column joints of frames at the base and at joints of coupled walls Spalling of concrete cover Buckling of steel rebars
Non-structural elements	Heavy damage/cracking	Failure of individual non-structural elements. Heavy damage or failure of façade arches or balconies Heavy damage to roof or ceilings	Large cracks in partition and infill walls Failure of individual infill panels Heavy damage of false ceilings
D4		Partial Structural Collapse	
Load bearing structural elements	Collapse of an individual floor or portion of building.	Serious failure of walls Partial structural failure of roofs and floors	Large cracks in structural elements Compression failure of concrete Fracture of rebars; Bond failure of beam rebars Tilting of columns Collapse of a few columns or a single upper floor
Non-structural elements	Very heavy damage/cracking		
D5		Full Structural Collapse	

* Classification is based on the main structure. Any appendages (e.g., an additional room built with masonry blocks on the roof) are not considered in the classification.

** Here, non-structural elements include partition walls, false ceilings, external cladding, balconies, facade arches, and exclude glazing, door and window frames, contents, or equipment.

Moreover, the 360° photos collected on October 8 and 15 (Section 4.2) were used to identify some of the more heavily damaged buildings (damage index D3 to D5) along the streets of the affected areas in Beirut, solely based on pictures from the exterior (the team did not visit these buildings).

In total, the combined efforts resulted in the assignment of a damage index to a total of 182 buildings. These buildings consist of 73 stone masonry bearing-wall buildings (for some of these buildings, concrete frames were later added within an existing floor or to build upper levels) and 109 reinforced concrete (RC) buildings. These buildings are located at blast distances of 0.6 to 4.4 km, with most being within 2 km.

4.3.2 Examples of Damaged Buildings

This section presents examples of buildings with different damage levels, as classified by the scheme in Table 4.3. The following section summarizes the main trends of the observed damage by location and structure typology.

Figure 4.4 shows the locations of example buildings that will be discussed here: stone masonry (SM) structures 1 to 9 and reinforced concrete (RC) buildings 1-3. Four of these structures are located close to each other at distances between 600 and 700 m from the blast (Figure 4.5) -- SM1, SM6, RC1 and RC2. They sustained different levels of damage, which are likely a consequence of their different structural typology and quality. Another possible factor is the presence of a direct line of sight from the blast, versus the line of sight being blocked by neighboring high-rise buildings.

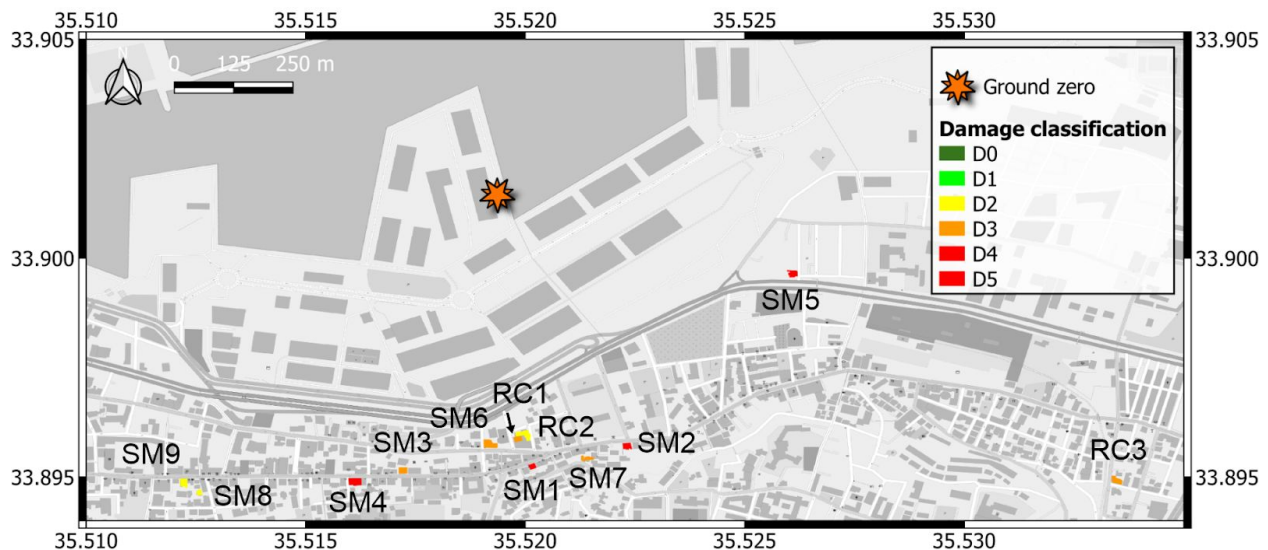


Figure 4.4. Locations of example stone masonry (SM) and reinforced concrete (RC) structures with varying levels of structural damage.

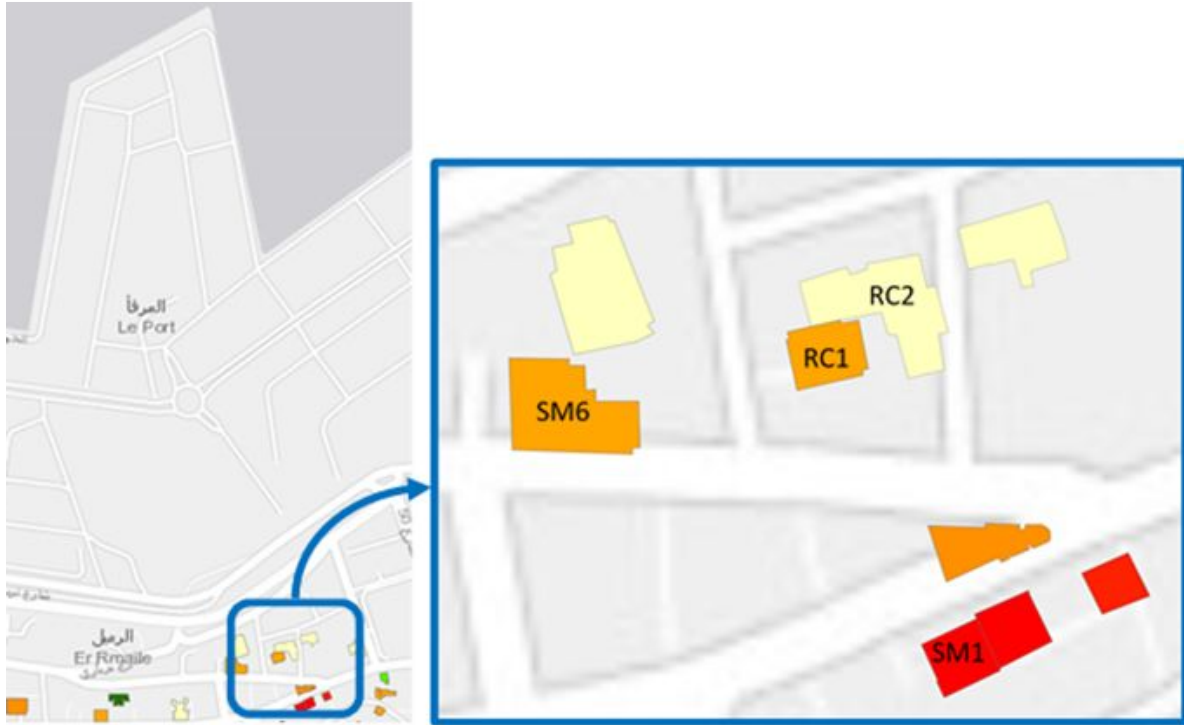


Figure 4.5. Set of buildings with varying structural typologies and damage classes.

Figure 4.6 shows three of the more heavily damaged stone masonry buildings classified based on 360° street scan photos and located at distances of 700-750 m from the blast. These buildings were not visited, but the 360° photos allowed for an approximate classification despite having no information on the state of their internal walls and back facades (not visible in the photos). Building SM1 was classified as D4-D5 because a major portion of the structure collapsed; see (a). Building SM2 was classified as D4 because part of the roof and part of the top floor have partially collapsed, and one of the exterior facades at the top floor exhibits a crack with significant deformation across it; see (b). Building SM3 was classified as D3-D4 because the roof and a portion of the external façade below the roof are partially collapsed and the balcony of the second floor is heavily damaged.



Figure 4.6. Heavily damaged stone masonry buildings classified based on 360 photos: (a) building SM1 (33.8952° N, 35.5202° E), D4-D5; (b) building SM2 (33.8956° N, 35.5223° E), D4; and (c) building SM3 (33.8953° N, 35.5172° E), D3-D4.

Figures 4.7 to 4.11 show pictures of stone masonry buildings located within 1 km from the blast and that were inspected from both the exterior and interior. SM4, shown in Figure 4.7, is a partially collapsed (D4) 4-story structure. Observations include partial collapse of the roof, heavy damage or collapse to some of the ceilings and interior partition walls, as well as some damage to the staircase and a façade column. SM5, shown in Figure 4.8, is a partially collapsed (D4) 3-story structure. Part of this structure was recently strengthened by adding a steel frame. The building sustained partial collapse only of the portion that was not strengthened, in addition to cracking in external walls and balcony failure. SM6, shown in Figure 4.9, is a heavily damaged (D3) 4-story building. Notable damages include cracking within and between stone masonry walls, separation between walls and slabs, permanent displacement of interior marble columns, and collapse of partition walls. Figure 4.10 shows another heavily damaged (D3) stone masonry building, SM7, which sustained extensive cracking in its walls, while Figure 4.11 shows some moderately damaged (D2) stone masonry buildings; SM8 sustained damage and partial failure of its roof, façade and balcony, while SM9 sustained some damage to its wooden roof truss.

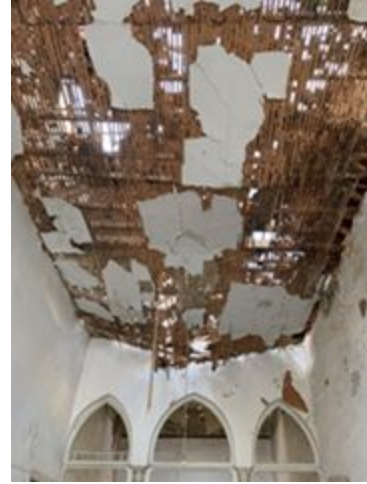


Figure 4.7. Partially collapsed (D4) stone masonry building SM4 (33.8948° N, 35.5161° E).



Figure 4.8. Partially collapsed (D4) stone masonry building SM5 (33.8996° N, 35.5260° E).



Figure 4.9. Heavily damaged (D3) stone masonry building SM6 (33.8958° N, 35.5192° E).



Figure 4.10. Another example of a heavily damaged (D3) stone masonry building SM7 (33.8954° N, 35.5214° E).

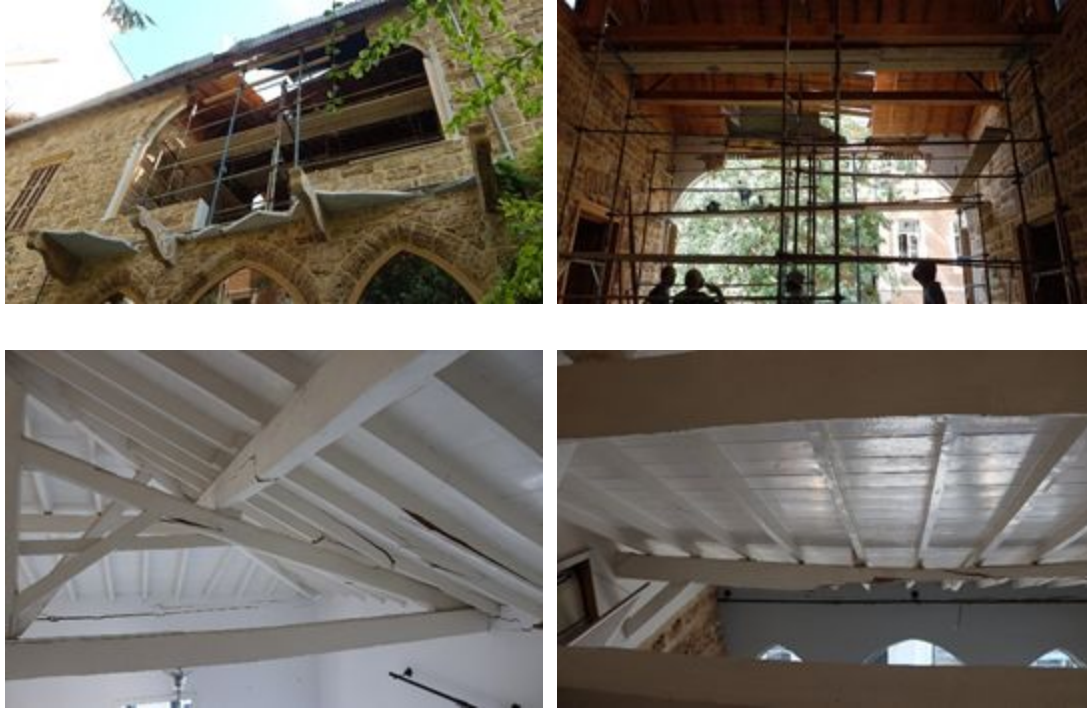


Figure 4.11. Example observations from moderately damaged (D2) stone masonry buildings: SM8 (33.8946° N, 35.5126° E) (top) and SM9 (33.8949° N, 35.5122° E) (bottom).

For RC buildings, some older gravity load designed buildings located within 1 km from the blast sustained heavy damage (D3), such as cracking and spalling in some concrete elements or large cracks in partition walls. RC1 is an example of a 5-story older reinforced concrete frame building located at about 650 m from the blast that sustained heavy damage (D3). As illustrated in Figure 4.12, observed damage includes cracking in concrete columns and at beam column joints, as well as large cracks or partial failure of partition walls and parapets.

As expected, the more recent seismically designed RC buildings had better structural performance than older gravity load designed RC buildings and sustained only light to moderate damage (D1 or D2), even at distances less than 700 m from the blast (e.g., building RC2; see Figure 4.13). However, unlike stone masonry and older RC buildings, which tend to have bare facades and ceilings, new/modern buildings have façade cladding, large bay windows and sliding aluminum door/frames and false ceilings. These non-structural elements sustained considerable damage in buildings located within 1 km from the explosion. RC2 is an example of a “modern” reinforced concrete building with shear walls, adjacent to RC1, also at about 650 m from the blast. Cracks were observed in partition walls but not in structural elements. The facades, cladding and false ceilings for that structure sustained heavy damage.

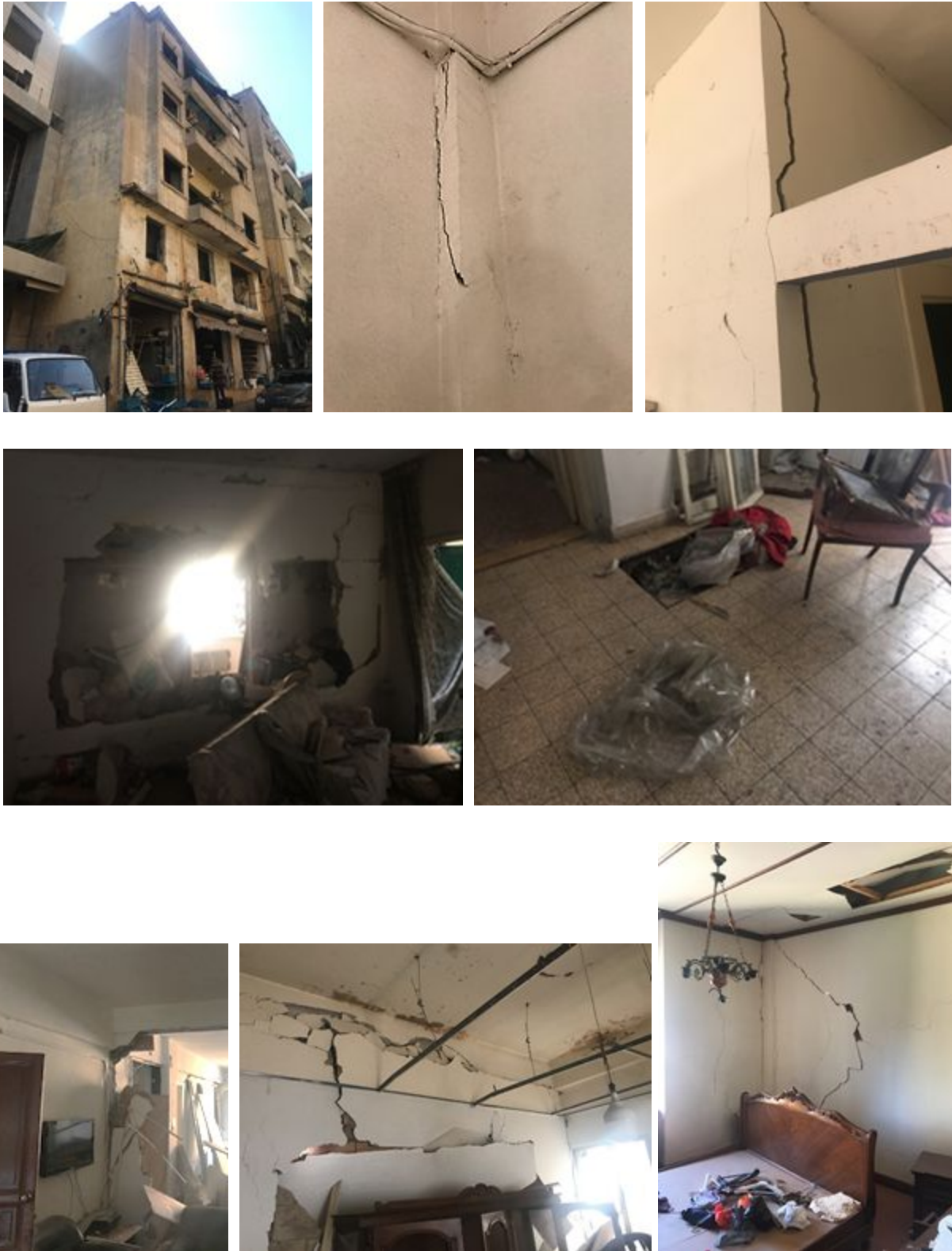


Figure 4.12. Heavily damaged (D3) older reinforced concrete building RC1 (33.8958° N, 35.5199° E).

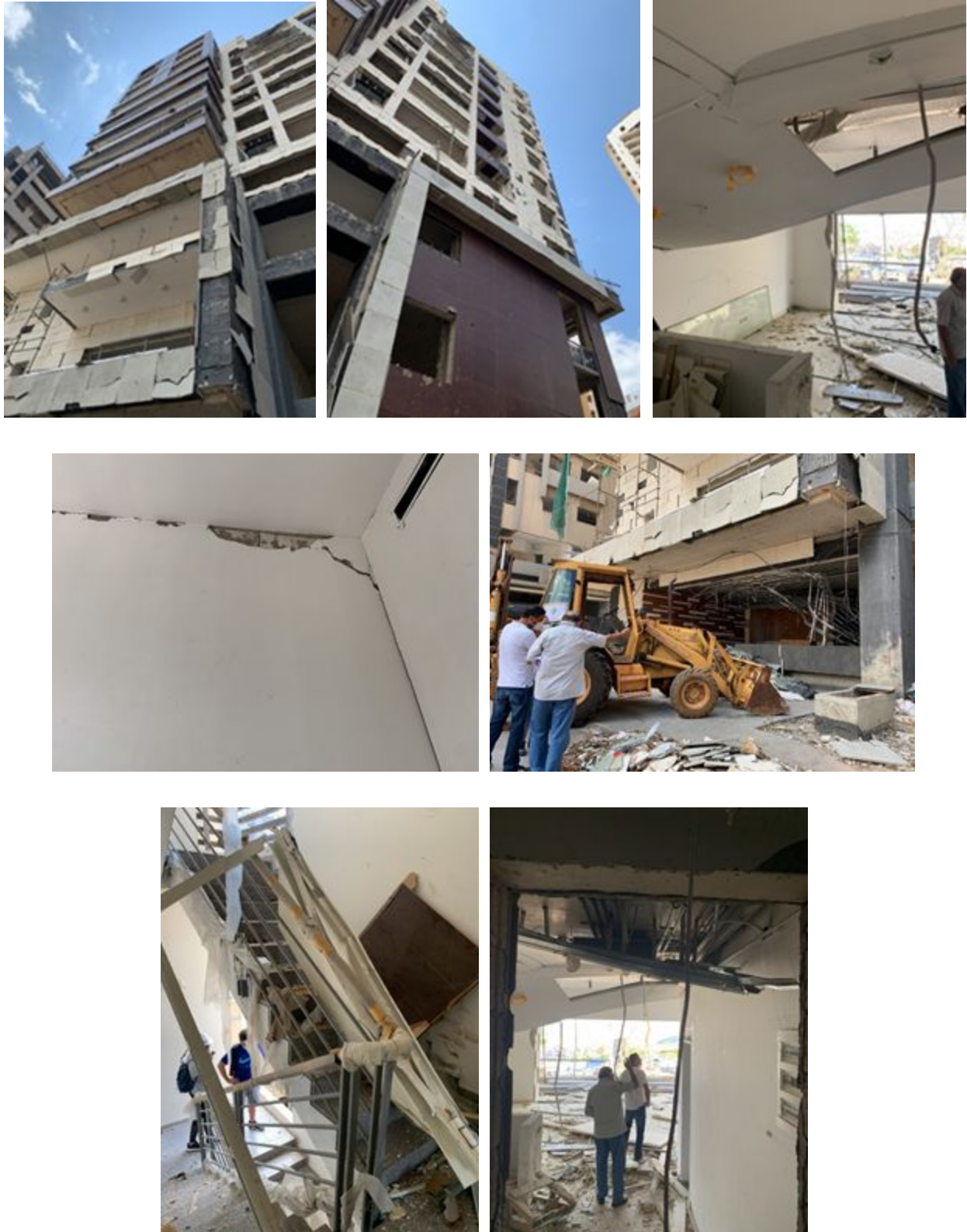


Figure 4.13. Moderately damaged (D2) new reinforced concrete building RC2 (33.8960° N, 35.5198° E).

A few RC buildings located at distances larger than 1 km sustained heavy damage (D3) because of their poor condition before the blast (pre-existing damage due to the Civil War and/or due to water leakages and corrosion). Beyond 2 km, RC buildings generally sustained no- to light-damage (D0 or D1). Figure 4.14 shows pictures taken during the inspection of RC3, a 4-story older RC frame building located 1.5 km from the blast. The condition of this building was poor before the blast, due to prior damage during the Lebanese Civil War (1975-1990) in addition to water leakage and heavy corrosion, which was further exacerbated by the blast. Some floor tiles at the building entrance caved in due to soil settlement. Moreover, cracking and spalling of concrete in beams and slabs occurred, facilitated by prior corrosion of steel. The upper level, which is not inhabited, already was in a poor condition that was then significantly worsened by the blast. The explosion heavily damaged one of its external hollow block walls; the wall partially collapsed and presents a risk of full collapse and therefore constitutes a hazard to the street below. Moreover, several cracks were observed in a number of the building's concrete columns and masonry walls.

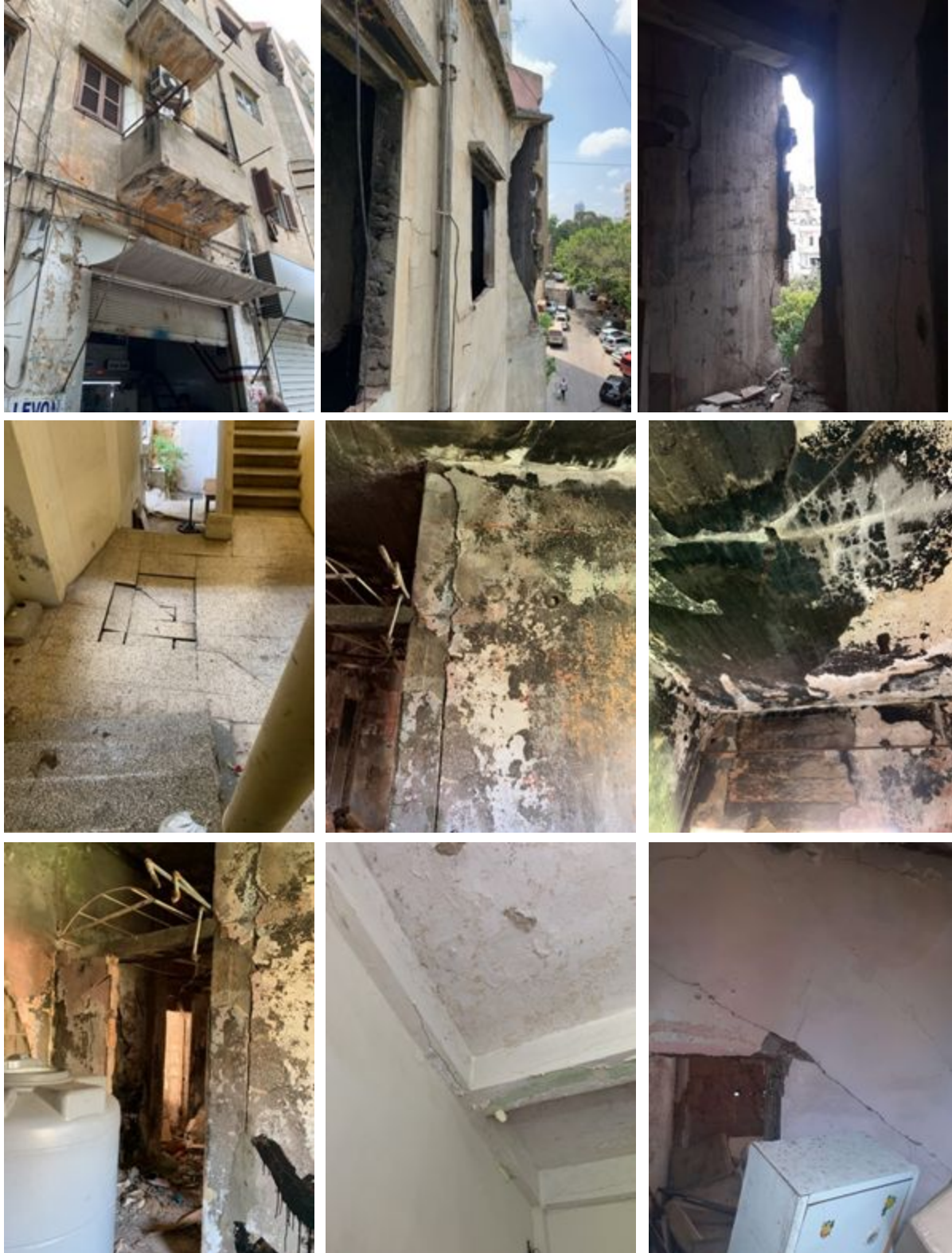


Figure 4.14. Heavily damaged (D3) older reinforced concrete building RC3 (33.8949° N, 35.5335° E) in poor condition before the blast.

4.3.3 Summary and Interpretation

The variability of the observed damage is mainly associated with the different structural typologies and the distance from the blast. As mentioned earlier, the in-person surveys were conducted in response to calls from residents or business owners concerned about the structural safety of their building. As a result, none of the buildings visited and inspected were fully collapsed, but a few of them were heavily damaged or partially collapsed. Ten more heavily damaged buildings were later identified from the street view photo survey.

The structures most damaged by the blast (D3, D4 and D5) were sandstone bearing-wall structures and older (gravity load designed) RC buildings located within 1.5 km of the blast. Modern RC structures located close to the blast suffered damage mostly to non-structural elements. More detailed observations and examples are provided in Section 4.3.2.

Figure 4.15(a) illustrates the distribution of damage classes D0 to D5 within stone masonry (SM) structures, whereas Figure 4.16(b) provides the same for RC buildings. It can be noted that the SM buildings generally suffered more damage than RC buildings. Moreover, none of the RC buildings assessed suffered partial or full collapse (D4 to D5). For the plots in Figure 4.15, intermediate damage categories (D0-D1, D1-D2, D2-D3 and D3-D4) were combined with their corresponding lower bound damage category, namely D0, D1, D2 and D3, respectively.

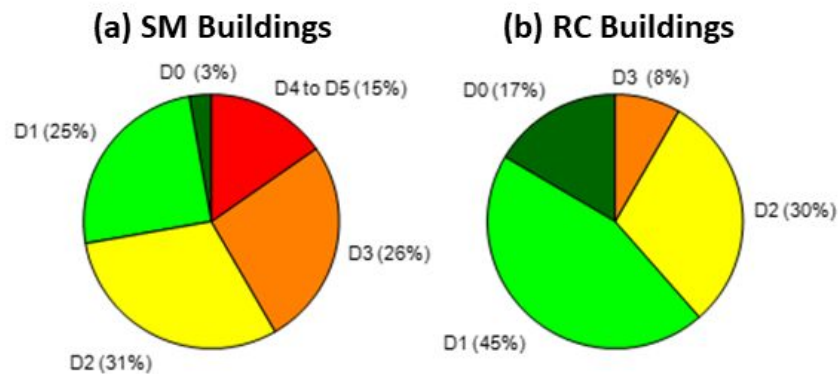


Figure 4.15. Distribution of damage classes in (a) Stone Masonry and (b) Reinforced Concrete buildings.

Figure 4.16 shows the distribution of damage classes D0 to D5 with distance from the blast. The top panels show histograms of the distances of the assessed buildings. The distributions are generally similar for both structural typologies, with most buildings within 2 km of the blast. The bottom panels show damage category versus distance for the two types of buildings. Figures 4.2(a) and (b) show that, in general, SM buildings suffered more damage than RC buildings at a similar distance from the blast. Moreover, SM buildings that sustained heavy damage or suffered partial or full collapse (damage categories D3 to D5) were located within 1 km from the blast. Those located at distances larger than 1 km sustained light to moderate

damage (D1 or D2), e.g. falling of pieces of plaster, some cracking in the walls, or some damage to façade arches, balconies, ceilings or roofs.

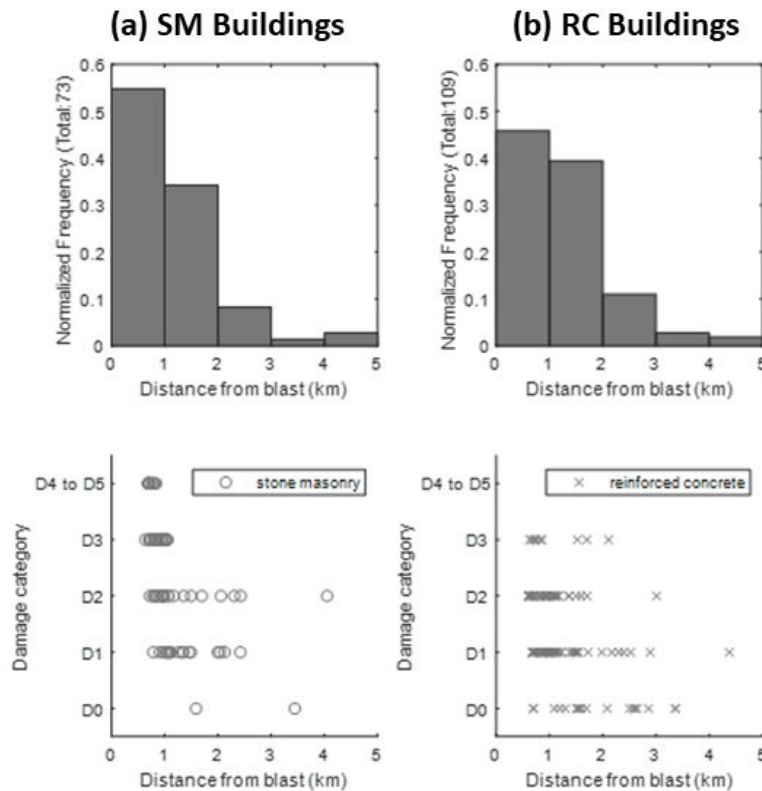


Figure 4.16. Top: Distribution of classified buildings with blast distance. Bottom: Blast distance dependence of damage categories. Part (a) corresponds to SM buildings and Part (b) to RC buildings.

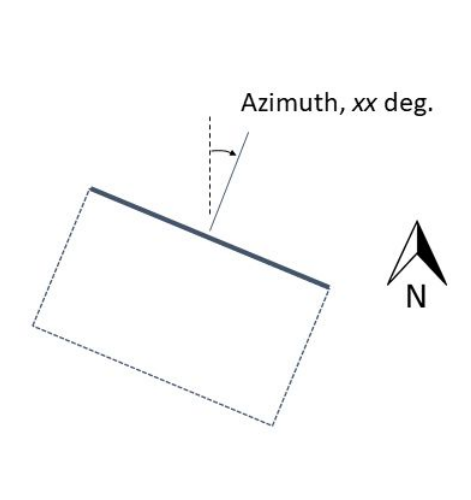
4.4 Façade Damage Assessment

4.4.1 Damage Classification

Using the ~2100 street view photos, we classified non-structural damage to building openings (windows, doors, and frames). This façade damage assessment was performed remotely by four different investigators. Consistency in the damage assessment process was ensured by regular meetings designed to minimize between-investigator discrepancies. The number of inspected facades is greater than the number of analyzed photos as one photo typically contained multiple facades belonging to different buildings. The damage assessment has been performed using QGIS and the results stored in a geodatabase. This non-structural damage assessment was performed using an *ad-hoc* damage classification specifically developed to study the impact of this explosion (Table 4.4). For each building façade inspected, the geodatabase we developed

contains: (1) damage classes, azimuth of the façade, break/blow-out rates (for damage classes 1 and 2), and comments on reconstruction activities taking place in the period between the explosion and dates when the photos were taken.

Table 4.4. Non-structural damage to building openings (windows/doors). These classifications are dependent on azimuth xx , as defined in the inset.

Façade Impact	Description	
Wxx-0	No observable effects on windows or doors	
Wxx-1-yy	Some windows broken, frames generally intact (yy% break rate). Doors remain in place	
Wxx-2-zz	Some window and door/door frames blown out (zz% blow-out rate)	
Wxx-3	Nearly complete blow-out of windows, doors, and their frames	

4.4.2 Results

Figure 4.17 shows example photos of facades experiencing non-structural damage classes Wxx-1 where damage was mainly related to broken windows (Figure 4.17a), Wxx-2 where windows were broken and frames were damaged (Figure 4.17b), and Wxx-3, the highest non-structural damage level, where there was complete blow-out of frames (Figure 4.17c). Photos shown in Figure 4.17 were taken in different districts of Beirut. Figure 4.18 shows the spatial distribution of façade damage in the analyzed area. Of the analyzed facades, ~5200 of them were classified as Wxx-0, ~1115 as Wxx-1, ~730 as Wxx-2, and ~1850 as Wxx-3. Figure 4.18 clearly shows that there is a clear fringe area that separates undamaged zones (Wxx-0) from zones with some damage ($Wxx > 1$). This fringe zone is located at a variable distance from the explosion. It is located at a distance of ~1.5km from the explosion in the Western part of Beirut. This distance becomes ~0.7km-0.9km in the central part of the city and becomes ~1.2km in the Eastern part of Beirut. This analysis suggests that there is a non-symmetric façade damage spatial distribution. It is possible that this pattern is related to the damping effect of tall buildings/structures and/or the different levels of structural vulnerability in different districts of the city.



Figure 4.17. Example of façade damage levels (a) Wxx-1: damage to windows only, (b) Wxx-2: damage to windows and frames, and (c) Wxx-3: complete blow-out of frames.

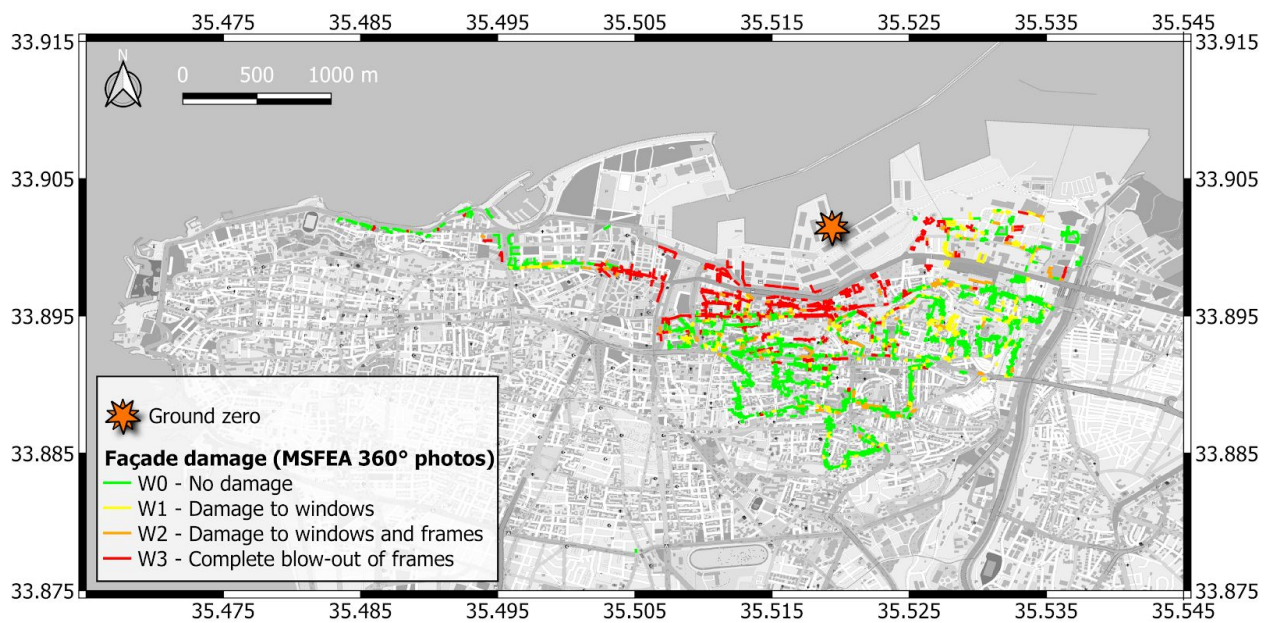


Figure 4.18. Non-structural damage assessment map.

4.5 Comparison of Damage Observations to DPMs

Figure 4.19 shows the DPM produced following the August 4 explosion along with structural damage levels (Table 4.3). Figure 4.20 shows a box and whisker plot highlighting how DPM correlates with structural damage; DPM in this plot has been converted to a numerical index between 0 and 1.0. This index corresponds to the colors on maps over the index range of 0.75-1.0, as shown in the plot (the index range of 0-0.75 produces no map coloration). In this plot, the two ends of the boxes represent the upper quartile (25% of the data is greater than this value) and lower quartile (25% of the data is smaller than this value), respectively, the line inside the box represents the median value, and two whiskers represent the minimum and maximum values within that category. The undamaged structures consistently occur at index values < 0.75 , and the damaged structures occur at index values > 0.75 , indicating that the DPM is effective at capturing incidents of structural damage. Among structures with damage (classes D1 to D5), DPM index is lowest for the low damage state D1 (median of about 0.8), approximately the same for D2 and D3 (median of about 0.85), and highest for D4-D5 (median > 0.9). This indicates an ability of DPM index to distinguish among damage levels.

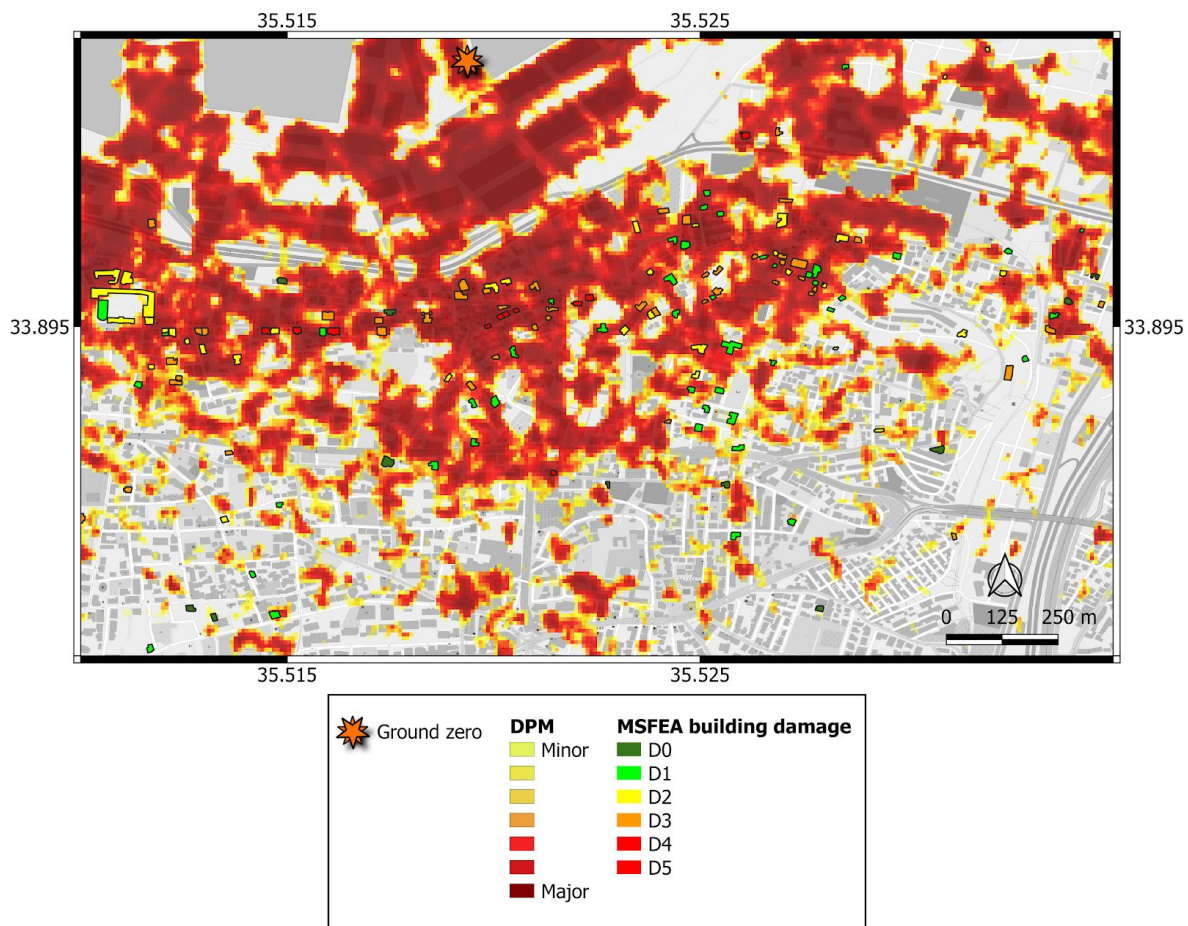


Figure 4.19. DPM and structural damage category distributions across Beirut.

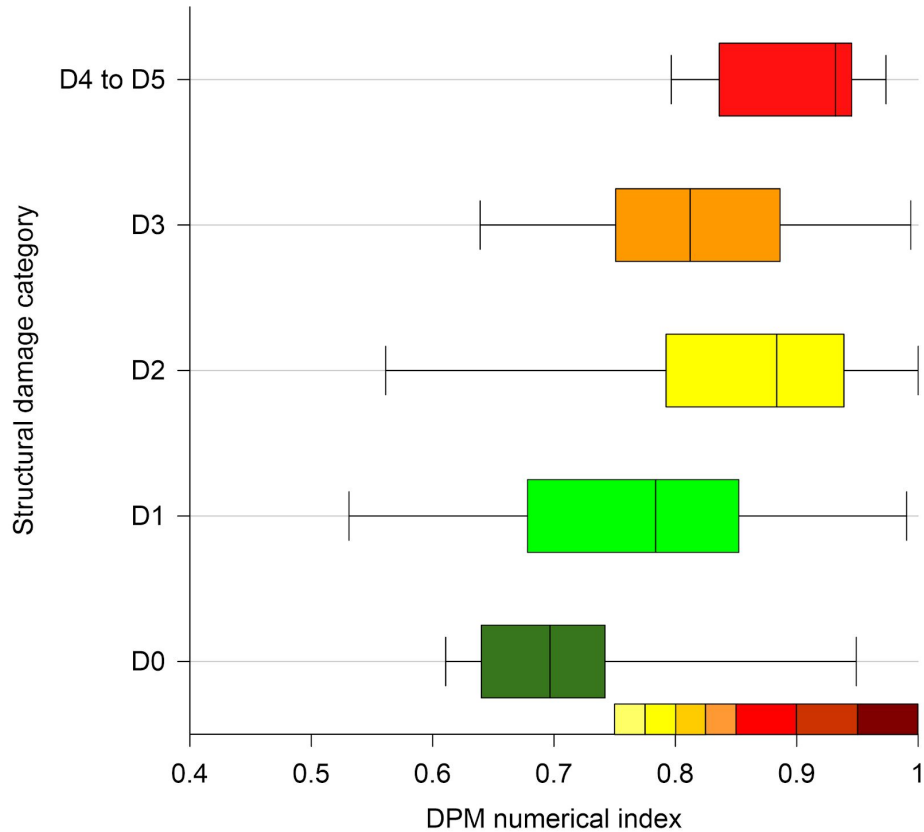


Figure 4.20. Relationship between numerical index of DPM (0-1) and structural damage categories

Figure 4.21 shows DPM along with façade damage levels (Table 4.4). The DPM seems to agree well with the overall non-structural damage pattern. The DPM identifies the fringe area separating the undamaged zone from the damaged area. The DPM also suggests high damage in the areas next to the blast source, within the Port and in the zone immediately outside of the Port zone. No street-view photos were available in this zone. However, the OEA damage maps clearly show that this zone was severely damaged by the explosion in all directions. Figure 4.22 shows a box and whisker plot highlighting how DPM correlates with non-structural damage. The correlation of facade damage with DPM is weaker than that for structural damage. The undamaged state (Wxx-0) has a median DPM index near the lower limit of shading (about 0.75). Among structures with non-structural damage, DPM index cannot distinguish between facade damage levels Wxx-1 and Wxx-2 (median DPM index of about 0.8), whereas the strongest level of damage (Wxx-3) has a clearly higher median DPM index of 0.9.

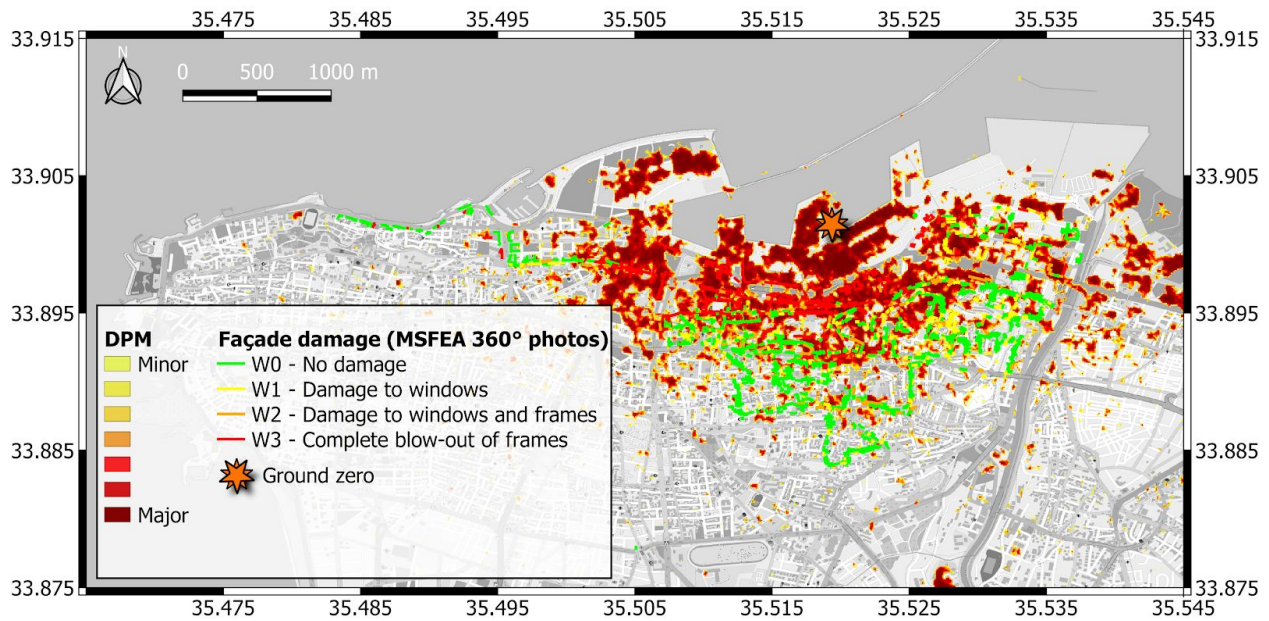


Figure 4.21. DPM and non-structural damage assessment map.

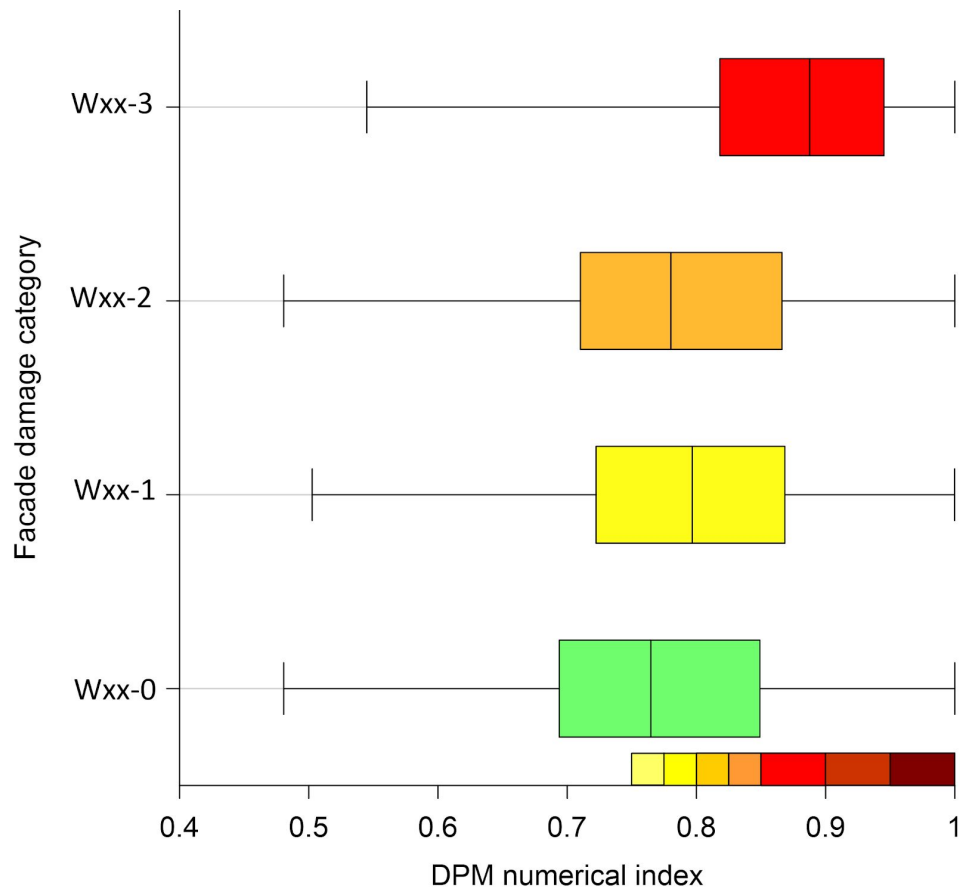


Figure 4.22. Relationship between numerical index of DPM (0-1) and non-structural damage categories.

5.0 Summary and Research Opportunities

The GEER reconnaissance presented in this report has compiled information on the effects of the disastrous 4 August 2020 explosion on Beirut infrastructure. We emphasize the impacts on the Port of Beirut where the explosion occurred and the building stock in the city up to a distance of approximately 4 km.

The impacts of the blast in the Beirut Port are documented to the quay walls and surrounding structures. The blast devastated a series of grain silos located as close as 50 m from the blast source, although a row of silos furthest from the blast source remains and was tilted towards the west (away from the blast). The blast created a crater up to 4-5 m in depth, a quay wall failure, and an apparent flow slide of poorly compacted silty sand fill material into Basin 3 adjacent to the failed quay wall.

In the City of Beirut, the blast produced varying levels of effects on buildings, from full collapse to facade damage at blast distances under 4 km. It is noteworthy that sporadic damage due to the blast extended to much farther distances in the form of broken windows and doors and impacting some facilities at the Beirut Rafic Hariri International Airport 8 km away from ground zero. We document both structural impacts and facade damage (mainly to windows and doors) as derived from structure-specific inspections and interpretation of street view imagery.

There are significant opportunities for additional data gathering and future research. Among these are:

1. Analysis of the blast impact on the silo structure to see if the observed collapses, and survivals, of particular silos is predictable. The permanent tilt of the silo foundations is also of interest with regard to modeling the impact on the soil-pile foundation system.
2. Analysis of the apparent flow slide to derive residual strengths, and pairing this with penetration resistance data for the remaining portions of the Port fill.
3. Follow up street-view imagery to monitor the recovery of the damaged sections of Beirut and the factors that influence the pace of that recovery.
4. Based on inspections and imagery from Order of Engineers surveys, the inventory of structures with classified structural damage can be expanded beyond the 182 presented here, albeit with increased uncertainty.
5. The factors affecting damage distributions in Beirut can be studied using hydro-dynamic simulations of the blast pulse through the city. Factors such as shielding of some portions of the city from tall intervening structures is a topic of particular interest.
6. Further analysis of DPM effectiveness regarding the damage from the blast and tracking of the recovery.

References

Applied Technology Council, ATC (1995). *ATC-20-2 Report, Addendum to the ATC-20 Postearthquake Building Safety Evaluation Procedures*.

Applied Technology Council, ATC (2004). *ATC-45 Field Manual: Safety Evaluation of Buildings after Windstorms and Floods*.

Bandera, M (2021). Beirut port silos scan reconstruction - 3D model, Silos Expertise Group, Lebanon Ministry of Commerce. [Link](#).

Beirut Order of Engineers and Architects, OEA (2020). *Beirut Port Explosion of Aug 04 2020: Buildings Final Structural Assessment Report*. OEA. Date: 12 Aug-17 September 2020.

Bray, J.D, J.P. Stewart (2000). Chapter 8: Damage patterns and foundation performance in Adapazari. Kocaeli, Turkey Earthquake of August 17, 1999 Reconnaissance Report, TL Youd, JP Bardet, and JD Bray, eds., *Earthquake Spectra*, Supplement A to Vol. 16, 163-189.

Council for Large Projects-Lebanese Ministry of Public Works (1970). Brochure on the occasion of the completion of works in the grain silos at the Beirut Port.

Diaz, J. S. (2020). Explosion analysis from images: Trinity and Beirut, Physics Education, <https://arxiv.org/abs/2009.05674>

Fielding, E.J., M. Talebian, P. A. Rosen, H. Nazari, A. Jackson, M. Ghorashi, and R. Walker (2005). Surface ruptures and building damage of the 2003 Bam, Iran, earthquake mapped by satellite Synthetic Aperture Radar interferometric correlation, *J. Geophys. Res.* 110, no. B03302.

Grünthal, G. (1998). European macroseismic scale 1998. European Seismological Commission (ESC).

Jung, J., S. Yun, S. (2020). Evaluation of coherent and incoherent landslide detection methods based on synthetic aperture radar for rapid response: A case study for the 2018 Hokkaido Landslides, *Remote Sensing*, **12**, 265, doi:10.3390/rs12020265, Jan 2020.

LIBNOR-Lebanese Standards Institution-(2013). Earthquake Loads: General Rules, NL 135: 2013 ed.2; ICS: 13.220.50

New York Times (2020). How a massive bomb came together in Beirut's Port. <https://www.nytimes.com/interactive/2020/09/09/world/middleeast/beirut-explosion.html>

Rathje, E.M., K. Franke (2016). Remote sensing for geotechnical earthquake reconnaissance, *Soil Dynamics and Earthquake Engineering*, **91**, 304-316.

Reuters Graphics (2020). How powerful was the Beirut blast.

<https://graphics.reuters.com/LEBANON-SECURITY/BLAST/yzdpxnmqbpv/>

Rigby, S.E., T.J. Lodge, S. Alotaibi, A.D. Barr, S.D. Clarke, G.S. Langdon, A. Tyas (2020). Preliminary yield estimation of the 2020 Beirut explosion using video footage from social media. *Shock Waves*, <https://doi.org/10.1007/s00193-020-00970-z>

Salameh, C., B. Guillier, J. Harb, C. Cornou, P.-Y. Bard, C. Voisin and A. Mariscal (2016). Seismic response of Beirut (Lebanon) buildings: instrumental results from ambient vibrations. *Bulletin of Earthquake Engineering* 14(10): 2705-2730.

Yun, S., E.J. Fielding, M. Simons, P. Rosen, S. Owen, and F. Webb (2011). Damage proxy map of February 2011 M 6.3 Christchurch earthquake using InSAR coherence, 8th International Workshop on Advances in the Science and Applications of SAR Interferometry, Frascati, Italy, 19–23 September 2011, [link](#). (last accessed Nov 2020).

Yun, S., K. Hudnut, S. Owen, F. Webb, M. Simons, P. Sacco, E. Gurrola, G. Manipon, C. Liang, E. J. Fielding, et al. (2015). Rapid damage mapping for the 2015 Mw 7.8 Gorkha earthquake using Synthetic Aperture Radar data from COSMO–SkyMed and ALOS-2 Satellites, *Seismol. Res. Lett.* **86**, 1549–1556.

Appendix

The forms used in the field surveys to assess structural and non-structural damage are presented here. Figure A.1 shows the main menu of the survey form on ArcGIS Survey123 (ESRI) as well as details of the *Assessment* section. Figure A.2 shows details of the *Building Identification* section. Figure A.3 shows details of the *Building Description*, *External Risk*, and *Damage Assessment* sections. Figure A.4 shows details of the *Structural Hazards* section. Figure A.5 shows details of the *Non-structural Hazards* section. Finally, Figure A.6 shows details of the *Overall Assessment*, *Further Actions*, and *End of Inspection Data Entry* sections.

The figure consists of two side-by-side screenshots of a mobile application interface for the MSFEA assessment form. Both screenshots show a status bar at the top with the time 4:42 and signal strength indicators. The header bar is green with a white 'X' icon on the left, the text 'MSFEA Response Hotline' in the center, and a white menu icon on the right. The left screenshot displays a list of menu items, each with a right-pointing arrow: 'Assessment *', 'Building Identification', 'Building Description', 'External Risk', 'Damage Assessment', 'Structural Hazards', 'Non-structural Hazards', 'Overall Assessment', 'Further Actions', and 'End of Inspection Data Entry'. A green checkmark is visible at the bottom right of the list. The right screenshot shows the 'Assessment' section expanded. It contains the following fields and options: 'Assessor Name *' with a text input field; 'Assessment Date *' with a date picker showing 'Tuesday, February 2, 2021'; 'Assessment time *' with a time picker showing '4:41 PM'; 'Areas Inspected *' with three radio button options: 'Exterior Only', 'Exterior & Interior', and 'Other'; 'The structure was previously assessed by another entity *' with three radio button options: 'Yes', 'No', and 'Unknown'; 'Prior assessment recommendation' with a text input field; and 'Prior assessment date' with a date picker showing 'Date'. A green checkmark is visible at the bottom right of the form.

Figure A.1. Part 1 of the MSFEA assessment form on ArcGIS Survey123 (ESRI)






MSFEA Response Hotline		
<p>▼ Building Identification</p> <p>Lot Number *</p> <p>Enter 0 if unknown</p> <input type="text"/>	<p>Building Address (Street Name)</p> <input type="text"/>	<p>MSFEA Hotline Call # *</p> <p>Enter 0 if unknown</p> <input type="text"/>
<p>How the lot number was obtained</p> <p> <input type="radio"/> Provided by tenant <input type="radio"/> Deduced from the map <input type="radio"/> Unknown </p>	<p>Location *</p> <p>33°53'N 35°31'E ± 65 m</p> 	<p>Contact Name *</p> <input type="text"/>
<p>Zone Name *</p> <p> <input type="radio"/> Achrafieh <input type="radio"/> Ain El Mreisse <input type="radio"/> Bachoura <input type="radio"/> Bourj_Hommoud <input type="radio"/> Mazraa <input type="radio"/> Medawar <input type="radio"/> Minet El Housn <input type="radio"/> Moussaytbeh <input type="radio"/> Port <input type="radio"/> Ras Beirut <input type="radio"/> Remeil <input type="radio"/> Saife <input type="radio"/> Zoukak El Blatt <input type="radio"/> Other </p>	<p>▼ Full Building Façade Photos</p> <p>Photos *</p> <p>Full Building Façade (for identification)</p> <div>   </div>	<p>Contact Phone Number</p> <input type="text"/>
<p>Building Name *</p> <input type="text"/>	<p>Photos</p> <p>Full Building Façade (for identification)</p> <div>   </div>	<p>Contact Type</p> <p> <input type="radio"/> Owner <input type="radio"/> Tenant <input type="radio"/> other </p>
		<p>Inhabited?</p> <p> <input type="radio"/> Yes <input type="radio"/> No </p>
		<p>Currently Vacated</p> <p> <input type="radio"/> Yes <input type="radio"/> No </p>
		<p>► Building Description</p>
		<p>► External Risk</p>
✓	✓	✓

Figure A.2. Part 2 of the MSFEA assessment form on ArcGIS Survey123 (ESRI)

4:43

MSFEA Response Hotline

Building Description

Stores Below Ground *

Stores above Ground *
Incl. ground floor

Number of Apartments

Approximate Footprint Area (m2) *

Approximate Total Area (m2) *

Building General Description

Primary Occupancy *

Residential

Commercial

Offices

Emergency Services

Hospital

Industrial

School

Government

Cultural

Public Assembly

Other

Secondary Occupancy
(e.g. shops)

Historic Building?

☐ Yes
☐ No

Construction Age *

☐ < 1935
☐ 1936-1955
☐ 1956-1975
☐ 1976-1990
☐ 1991-2005
☐ > 2006
☐ Other

Main Structure Type *

☐ Reinforced concrete frame
☐ Reinforced concrete walls
☐ Stone masonry bearing walls
☐ Steel
☐ Other

Other Structural Systems

Cladding type

☐ Brick veneer
☐ Concrete panels
☐ Sheet material
☐ Weatherboard
☐ Exterior Insulation Finishing System
☐ Other

4:44

MSFEA Response Hotline

External Risk

Objects falling from adjacent buildings?

☐ Yes
☐ No

Adjacent Building address

Damage Assessment

Collapse or partial collapse *

☐ Minor or None
☐ Moderate
☐ Severe
☐ Other

Building or Storey Leaning *

☐ Minor or None
☐ Moderate
☐ Severe
☐ Other

Photos
Damage Assessment

Photos
Damage Assessment

Figure A.3. Part 3 of the MSFEA assessment form on ArcGIS Survey123 (ESRI)

71

4:45 MSFEA Response Hotline

▼ Structural Hazards

Select all your structural hazard observations

- ☐ Foundations
- ☐ Floors
- ☒ Walls
- ☒ Columns
- ☐ Roofs and Ceilings
- ☐ Diaphragms and bracing
- ☐ Connections

Walls

- ☐ Minor or None
- ☐ Moderate
- ☐ Severe
- ☐ Other

Columns

- ☐ Minor or None
- ☐ Moderate
- ☐ Severe
- ☐ Other

4:45 MSFEA Response Hotline

Further Structural Comments

Other Note

▼ Structural Hazards Photos

Photos

Photos

Photos

Photos

✓ ✓

Figure A.4. Part 4 of the MSFEA assessment form on ArcGIS Survey123 (ESRI)

4:46 MSFEA Response Hotline

Overall Assessment

Final Posting *

☐ None

☐ Green (Inspected)

☐ Yellow (Restricted use)

☐ Red (Unsafe)

Estimated Building Damage

☐ 0-11%

☐ 11-31%

☐ 31-61%

☐ 61-100%

Further Actions

Barricades needed

☐ Yes

☐ No

Areas to Barricade

Partial or full scaffolding needed?

☐ Yes

☐ No

Areas to Scaffold

Detailed Structural Evaluation Recommended?

☐ Yes

☐ No

Possible Further Actions

☐ Yes

☐ No

Other Recommendations

End of Inspection Data Entry

Data entry completed

☐ Yes

☐ No

Date

Completed by

Figure A.6. Part 6 of the MSFEA assessment form on ArcGIS Survey123 (ESRI)